© 2018. Published by The Company of Biologists Ltd | Development (2018) 145, dev162115. doi:10.1242/dev.162115

RESEARCH ARTICLE

ROCK-nmMyoII, Notch and *Neurog3* gene-dosage link epithelial morphogenesis with cell fate in the pancreatic endocrine-progenitor niche

Eric D. Bankaitis*, Matthew E. Bechard, Guoqiang Gu, Mark A. Magnuson and Christopher V. E. Wright‡

ABSTRACT

During mouse pancreas organogenesis, endocrine cells are born from progenitors residing in an epithelial plexus niche. After a period in a lineage-primed *Neurog3*^{LO} state, progenitors become endocrine committed via upregulation of *Neurog3*. We find that the *Neurog3*^{LO} to *Neurog3*^{HI} transition is associated with distinct stages of an epithelial egression process: narrowing the apical surface of the cell, basalward cell movement and eventual cell-rear detachment from the apical lumen surface to allow clustering as nascent islets under the basement membrane. Apical narrowing, basalward movement and *Neurog3* transcriptional upregulation still occur without Neurog3 protein, suggesting that morphogenetic cues deployed within the plexus initiate endocrine commitment upstream or independently of Neurog3. Neurog3 is required for cell-rear detachment and complete endocrine-cell birth. The ROCK-nmMyoII pathway coordinates epithelial-cell morphogenesis and the progression through *Neurog3*-expressing states. NmMyoII is necessary for apical narrowing, basalward cell displacement and *Neurog3* upregulation, but all three are limited by ROCK activity. We propose that ROCK-nmMyoII activity, *Neurog3* gene-dose and Notch signaling integrate endocrine fate allocation with epithelial plexus growth and morphogenesis, representing a feedback control circuit that coordinates morphogenesis with lineage diversification in the endocrine-birth niche.

KEY WORDS: Plexus, Organogenesis, Morphogenesis, Differentiation, Progenitor, Niche

INTRODUCTION

In mouse pancreatogenesis, tissue growth, morphogenesis and differentiation must be coordinated, although how remains largely unresolved. We have reported that bipotent duct and endocrine progenitors exist within an epithelial niche called the 'plexus state' (Bankaitis et al., 2015), which comprises a web-like epithelium arising around E12.5 within an anlage of multipotent progenitors (MPC) (Kesavan et al., 2009; Hick et al., 2009; Villasenor et al., 2010). From E12.5-18.5, the plexus undergoes rapid expansion and remodeling, very different from classical branching morphogenesis, concurrent with a prolonged wave of endocrine-cell birth (Pan and Wright, 2011). The progressive replacement of plexus by an arbor-like ductal epithelium is associated with a great reduction in the production of new endocrine cells (Kopp et al., 2011; Bankaitis et al., 2015). Here, we investigate the coordination of plexus morphogenesis and endocrine cell-fate allocation.

Pancreatic endocrine cells derive from a Notch-responsive Sox9^{+} progenitor pool (Apelqvist et al., 1999; Kopp et al., 2011; Serup, 2012) via activation of the endocrine-lineage determinant neurogenin 3 (*Neurog3*; Gradwohl et al., 2000; Schwitzgebel et al., 2000; Gu et al., 2002). *Neurog3* is necessary and sufficient for endocrine-cell birth (Gradwohl et al., 2000; Johansson et al., 2007). Cells with high-level *Neurog3* (*Neurog3*^{HI}) exit the cell cycle (Miyatsuka et al., 2011), egress from the epithelium (Gouzhi et al., 2011) and cluster adjacent to the forming nascent islets of Langerhans. Lineage tracing in *Neurog3*-null and hypomorphic mice (Wang et al., 2010; Shih et al., 2012) showed that preventing acquisition of the *Neurog3*^{HI} state causes cells to remain intra-epithelial and to differentiate into mature acinar and ductal fates. The mechanisms regulating progression of epithelial progenitors through various *Neurog3* expression states are poorly defined.

Non-autonomous feedback from *Neurog3*-expressing cells regulates numerous processes in forming duct versus endocrine tissues. Inactivating *Neurog3* greatly expands low-level *Neurog3* (*Neurog3*^{LO}) transcription throughout the Sox9^{+} epithelium and causes the loss of *Neurog3*^{HI} cells (Wang et al., 2010; Bechard et al., 2016). *Neurog3* loss causes a widespread reduction in epithelial Notch-pathway activity (Magenheim et al., 2011; Shih et al., 2012; Qu et al., 2013). Thus, *Neurog3*^{HI} cells normally induce lateral inhibition of *Neurog3* expression in surrounding Sox9^{+} progenitors to balance endocrine differentiation with progenitor maintenance (Afelik et al. 2012; Qu et al., 2013; Apelqvist et al., 1999; Murtaugh et al., 2003). *Neurog3* deficiency causes a persistent reduction in Sox9^{+} cell replication, suggesting additional functions in supporting replicative growth of progenitor epithelium (Bankaitis et al., 2015). *Neurog3* loss results in a dysmorphic plexus that is precociously transformed into more-mature epithelial duct and branched states, again suggesting that egressing endocrine cells modulate normal morphogenesis by maintaining their parental 'plexus niche' (Magenheim et al., 2011; Bankaitis et al., 2015). Collectively, these studies position *Neurog3*-expressing cells as a coordination nexus for progenitor maintenance, cell-fate allocation and plexus morphogenesis, to regulate growth and assembly of the ductal network with formation of a dispersed endocrine pancreas (Rieck et al., 2012; Bankaitis et al., 2015).

In epithelia, the molecular motor nmMyoII acts on filamentous-actin (F-actin) substrates in apical constriction, tissue folding, cell delamination and migration, and generation of inter- and intra-cellular tension (Gorfinkiel and Blanchard, 2011; Heisenberg and

Vanderbilt University Program in Developmental Biology, Department of Cell and Developmental Biology, Vanderbilt Center for Stem Cell Biology, Vanderbilt University, Nashville, TN 37232, USA.
*Present address: Center for Gastrointestinal Biology and Disease, University of North Carolina School of Medicine, Chapel Hill, NC 27516, USA.

‡Author for correspondence (chris.wright@vanderbilt.edu)

C.V.E.W., 0000-0002-9260-4009

Received 29 December 2017; Accepted 3 August 2018

Development (2018) 145, dev162115. doi:10.1242/dev.162115

Bellaïche, 2013; Martin and Goldstein, 2014). Rho-associated kinase (ROCK) positively regulates nmMyoII activity (Wang et al., 2009), but also functions as a modulator of actin remodeling (Watanabe et al., 1999; Maekawa et al., 1999; Reinto and Ridley, 2003), affecting tissue and cell-shape change, cell polarization and migration (Li et al., 2005; Nakayama et al., 2005, 2008). ROCK-nmMyoII activities influence many complex morphogenetic and intracellular signaling processes (Amano et al., 2010). Rho-GTPase signaling, an upstream ROCK/nmMyoII regulator, influences neural-crest specification in frog embryos (Kim et al., 2015), and specific cell-fate decisions in mesenchymal cells (Sordella et al., 2003; McBeath et al., 2004). These reports clearly point to integration between morphogenesis signaling and the intrinsic gene-regulatory networks that drive cell fate.

We report here on the mechanistic interconnections between epithelial morphogenesis and fate in the pancreatic plexus niche. We use three-dimensional tissue reconstructions, gene-reporter analyses and genetic and pharmacological interventions to study interdependencies between *Neurog3* gene activity, Notch signaling and ROCK nmMyoII-controlled epithelial-cell morphogenesis. We propose that sequential, dissociable steps in endocrine fate allocation are mediated by morphogenetic changes at an apical versus basal cell surface. *Neurog3*^{LO} expression initiates concurrently with apical surface contraction, and becomes upregulated as its apical surface becomes increasingly focalized and the cell begins basalward movement. Initial contraction, focalization and *Neurog3* upregulation occur in the absence of Neurog3 protein, suggesting that endocrine specification and entry to commitment occur via epithelium-intrinsic inputs upstream or independent of Neurog3. nNmMyoII and ROCK oppositely regulate apical narrowing, focalization and basalward cell movement, and thus acquisition of the *Neurog3*^{HI} state. We propose a model in which a circuit comprising ROCK-nmMyoII, *Neurog3* gene dosage and Notch signaling balances apportionment of endocrine cells from the plexus while enabling proper growth and morphogenesis of the pancreatic epithelium.

RESULTS

Morphological transitions of the F-actin^{+} apical cortex are associated with cell-fate determination

A prominent feature in polarized epithelial cells is a belt of filamentous actin (F-actin) circumscribing the sub-apical cell cortex (Martin and Goldstein, 2014). These belt-like structures (hereafter F-actin^{BELT}) are closely apposed to tight and adherens junctions, and are important in mediating remodeling processes such as apical constriction, tissue folding, cell intercalation and epithelial egress or extrusion, among others (Heisenberg and Bellaïche, 2013). To probe whether specific cell-shape changes are associated with duct versus endocrine cell-fate decisions, we compared the F-actin^{BELT} topologies in cells located within the endocrine progenitor-rich plexus, the endocrine progenitor-poor duct state and in cells expressing *Neurog3* using an EGFP knock-in null allele (Lee et al., 2001). For the plexus, confocal *z*-stack reconstructions showed an intense multicellular meshwork of cortical F-actin closely associated with the Muc1^{+} apical lumen surface (Fig. 1A). The F-actin^{BELT} was located nearby the apical ZO1^{+} tight junctions, near the apical-most extent of Ecad^{+} adherens junctions, and apical with respect to the nuclei of all epithelial cells (Fig. S1A-H′ and data not shown), as expected for F-actin^{BELT} in most epithelia. Plotting the F-actin^{BELT} aspect ratio against F-actin^{BELT} perimeter length from many individual cells served as a metric of apical surface shape (Fig. S2A-B) and revealed a spectrum of apical surface shapes in *Neurog3*$^{+/+}$ and heterozygous-null *Neurog3*$^{EGFP/+}$ plexus (Fig. 1D). This spectrum in the plexus was similar throughout mid-to-late gestation, indicating that the overall mix of topologies is maintained during the major wave of cellular differentiation (Fig. 1E). Also in the plexus, numerous intense F-actin puncta were located directly at the Muc1^{+}aPKC^{+} lumenal surface, in a highly focalized pattern (hereafter, F-actin^{FOCAL}), signifying tightly narrowed apical contacts or tethering points (Bechard et al., 2016) of egressing *Neurog3*-expressing cells (Fig. 1B,C; Fig. S3A-D). Essentially all Muc1^{+} cells expressing *Neurog3*^{EGFP} exhibited a narrowed F-actin^{BELT} or F-actin^{FOCAL} signal (Fig. 1F). In contrast, the F-actin^{BELT} of essentially all cells in the duct state exhibited a larger perimeter and decreased aspect ratio (Fig. 1G-J). Scoring E-cad^{+} cell boundaries near the apical surface of these cells confirmed a large apical domain (Fig. S4A-D) and cell-flattening phenotype consistent with ductal differentiation (Grapin-Botton, 2005). In duct-state epithelium, *Neurog3*-reporting cells and F-actin^{FOCAL} structures were reduced or absent compared with plexus, consistent with a large reduction in Neurog3^{+} cell numbers (Bankaitis et al., 2015). EGFP-expressing cells without Muc1^{+} apical lumen-contact were considered to have exited the epithelium as endocrine-committed cells, and were not investigated further. These analyses suggest that F-actin^{BELT} narrowing and F-actin^{FOCAL} formation are associated with activation of *Neurog3* expression, while the larger F-actin^{BELT} shapes are associated with ductal or non-endocrine cell fates.

Morphogenetic influences mediate endocrine commitment in the plexus upstream of Neurog3 protein

In E14.5 *Neurog3*^{NULL} (*Neurog3*$^{EGFP/EGFP}$) epithelium, *Neurog3*^{HI} (EGFP^{HI}) cells are lost, *Neurog3*^{LO} (EGFP^{LO}) cell numbers are increased, and the epithelial plexus is dysmorphic (Wang et al., 2010; Magenheim et al., 2011; Bankaitis et al., 2015; Bechard et al., 2016). Accordingly, we observed a dramatic loss of Muc1^{+}F-actin^{FOCAL} structures, and a shift in apical F-actin^{BELT} shapes toward a more uniform circular morphology relative to *Neurog3*$^{+/+}$ and *Neurog3*$^{EGFP/+}$ samples (Fig. 2A-D,I). In addition to the previously reported ‘epithelial fattening’ observed in the *Neurog3*^{NULL} state, we also detected increased numbers of Sox9^{+} nuclei per unit of Muc1^{+} epithelium (Fig. S5A,B), consistent with a relative cell-crowding effect caused by the lack of egress of endocrine-committed cells. Although not establishing cause and effect, these data show that multiple morphological features of the plexus state, including apical F-actin^{FOCAL} structures formed in *Neurog3*^{HI} cells, are altered or lost in the absence of Neurog3 function.

We recently reported that the abnormal E14.5 *Neurog3*$^{EGFP/EGFP}$-null epithelium undergoes a delayed morphological compensation during late gestation (E16.5-18.5) to adopt an epithelial branched structure highly similar in gross morphology to controls (Bankaitis et al., 2015). This ‘corrective remodeling’ process provides a stringent model to assess whether *Neurog3* promoter activity, which is reduced and expanded across the abnormal E14.5 *Neurog3*$^{EGFP/EGFP}$ plexus, can be stimulated by Neurog3-independent cues that regulate the late-stage remodeling of the plexus to a more regular epithelial tree. Numerous inspections of E17.5 and E18.5 thick-sectioned and Muc1-labeled *Neurog3*$^{EGFP/EGFP}$ pancreata confirmed epithelial remodeling to the grossly wild-type relative proportions of plexus, duct and branched states (Fig. S6A-D). The number of Sox9^{+} nuclei per linear unit of Muc1^{+} epithelium was comparable in E17.5 control and *Neurog3*$^{EGFP/EGFP}$ plexus (Fig. S5B), in contrast to the increased cell density in E14.5

Development (2018) 145, dev162115. doi:10.1242/dev.162115

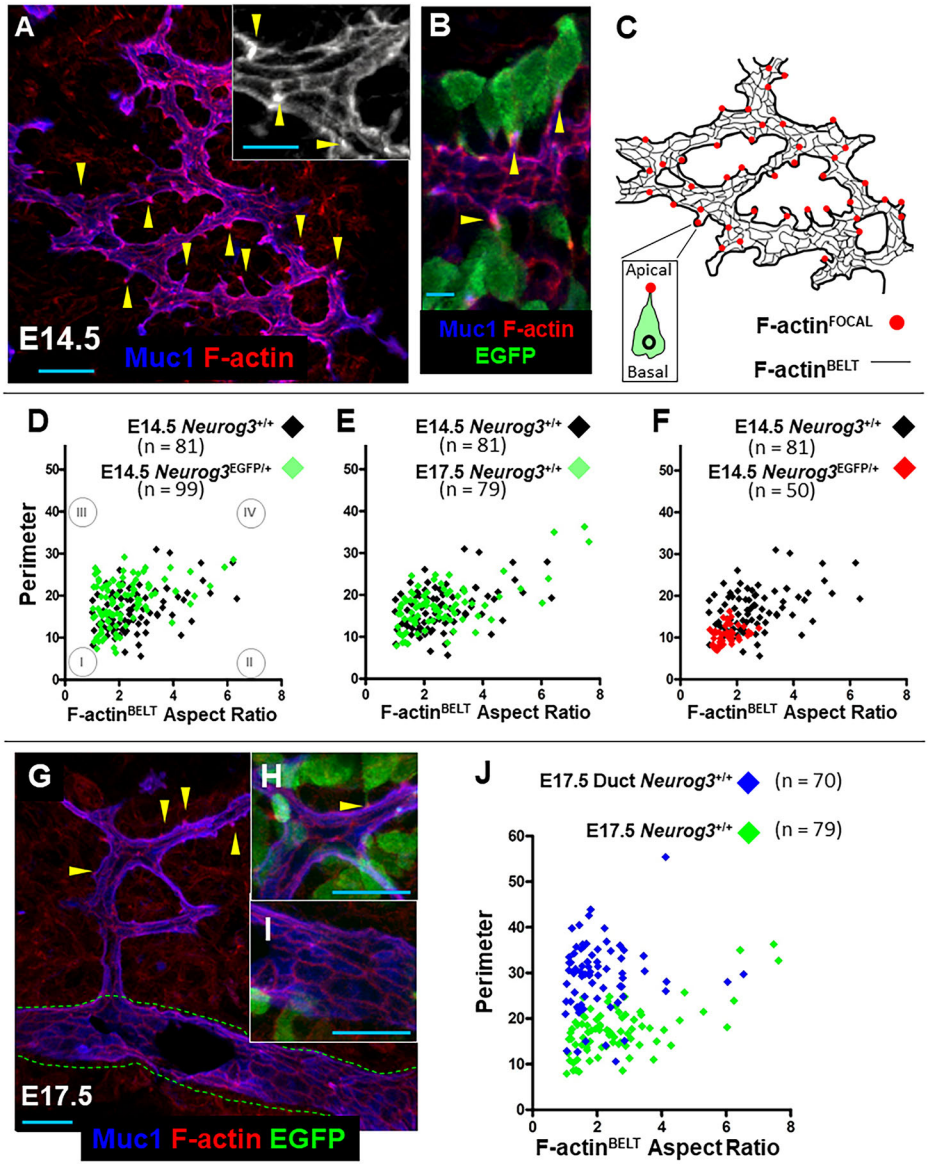

Fig. 1. Duct versus endocrine differentiation is associated with apical expansion or narrowing of the F-actin^{+} cell cortex. (A) Confocal *z*-stack (30 µm depth) of E14.5 dorsal pancreas showing plexus labeled with Muc1 and F-actin. Inset shows cortical F-actin (F-actin^{BELT}) in individual epithelial cells. (B) F-actin^{FOCAL} marks the apical-lumen contacts of egressing *Neurog3*$^{EGFP/+}$ EGFP^{+} cells. (C) Manual trace of F-actin^{BELT} meshwork (thin black lines) from A showing F-actin^{FOCAL} structures (red dots) and *Neurog3*-expressing cells (inset). (D) Cortical F-actin^{BELT} aspect ratio versus perimeter of *n* cells (at least three separate samples) for control or *Neurog3*$^{EGFP/+}$ cells randomly selected from E14.5 plexus. I, narrowed F-actin^{BELT}; II, elongated F-actin^{BELT}; III, expanded F-actin^{BELT}; IV, expanded and elongated F-actin^{BELT}. These indicators apply to E, F and J. (E) F-actin^{BELT} distributions from E14.5 and E17.5 *Neurog3*$^{+/+}$ plexus. (F) F-actin^{BELT} shape spectrum from E14.5 wild-type plexus and apically narrowed *Neurog3*-expressing cells from *Neurog3*$^{EGFP/+}$ plexus. (G) Confocal *z*-stack (30 µm) of representative plexus and duct states at E17.5; duct state indicated by dashed green line. Yellow arrowheads indicate F-actin^{FOCAL} structures in A, B and G. (H,I) Enlargements of the plexus and duct state in G. F-actin^{BELT} is expanded and there is a lack of F-actin^{FOCAL} in the duct state. (J) F-actin^{BELT} shape spectrum from E17.5 plexus and duct states. Scale bars: 20 µm in A,G-I; 5 µm in B.

Neurog3$^{EGFP/EGFP}$ plexus. Moreover, the spectrum of apical surface shapes within the E17.5 plexus of *Neurog3*$^{EGFP/EGFP}$ samples was essentially indistinguishable from controls (Fig. 2E,G,J). Thus, multiple aspects of the abnormal morphogenesis in *Neurog3*^{NULL} tissue at E14.5 were corrected by late gestation. Surprisingly, such corrected plexus also displayed periodically spaced *Neurog3*$^{EGFP\text{-}HI}$ cells (Fig. 2F,H), with narrowed F-actin^{BELT} structures at their apical surface (not shown). Although the EGFP^{HI} cell number in late-stage *Neurog3*$^{EGFP/EGFP}$ plexus was reduced compared with control (quantified below), these data indicate that defects in *Neurog3* transcriptional upregulation are substantially bypassed, independently of Neurog3 protein function, when the *Neurog3*$^{EGFP/EGFP}$ plexus undergoes corrective remodeling. This effect was essentially specific for cells in the plexus state, because very few EGFP^{HI} cells were observed in non-plexus ductal or branched states, which is the case for normal ductal and branched state (Fig. 5C-D; Fig. S6A-D). These data suggest that morphogenetic cues deployed within a 'normal' remodeling plexus can profoundly influence *Neurog3* levels, and that some initial steps in endocrine-cell commitment are initiated in part through *Neurog3*-independent pathways (Fig. 2K,L).

Apical narrowing, focalization and basalward cell displacement mark the endocrine-committed state

To study how particular morphogenetic inputs could be linked to the progression of cells through *Neurog3*-expressing states, we focused on the morphological alterations occurring as epithelial (Muc1^{+}) *Neurog3* expression is activated and upregulated during endocrine-cell birth. In E14.5 *Neurog3*$^{EGFP/+}$ pancreata, we observed Muc1^{+}EGFP^{LO} cells (6.5% of Muc1^{+}EGFP^{+} cells, n=95; Fig. S7A,C) without a narrowed or focalized apical surface (Fig. 3A,A′). Another 19.3% of Muc1^{+}EGFP^{+} cells showed a narrowed but not focalized apical surface, and all were EGFP^{HI} (Fig. 3B,B′). The majority (74.2%) of Muc1^{+}EGFP^{+} cells exhibited clear apical focalization, and again all were EGFP^{HI}. The mean *Neurog3*^{EGFP} intensity of apically non-narrowed, narrowed and focalized Muc1^{+}EGFP^{+} cells indicated a strong link between narrowing and focalization and the EGFP^{HI} state (Fig. 3E; Fig. S7C). The majority of Muc1^{+}EGFP^{HI} cells with a focalized apical surface also showed a basalward displacement of the cell body – assessed as a displaced nuclear location relative to the Muc1^{+} epithelial plane – and indications of basal-surface ruffling and protrusive distortions shown in our previous publications to

Development (2018) 145, dev162115. doi:10.1242/dev.162115

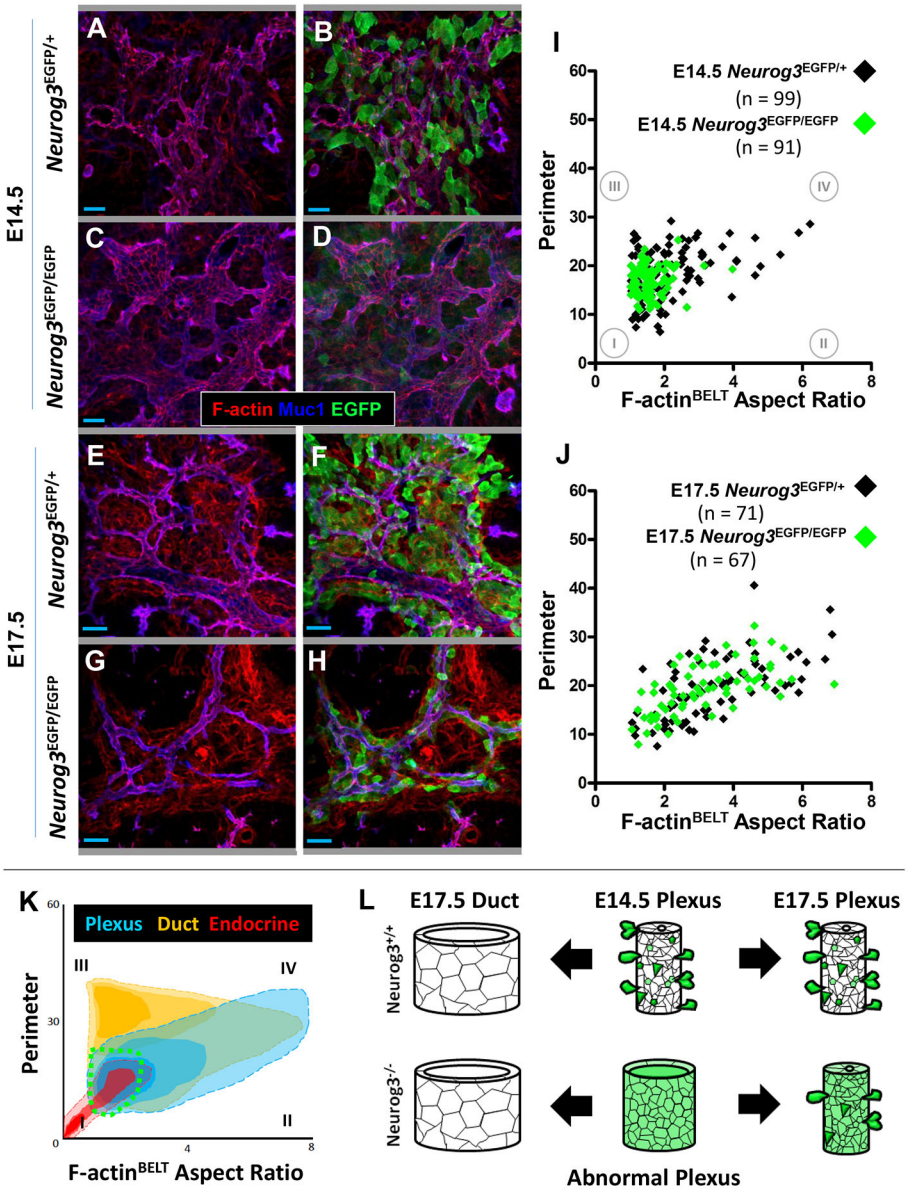

Fig. 2. *Neurog3* upregulation in *Neurog3* nullizygous plexus. (A-D) *Neurog3*$^{EGFP/+}$ versus *Neurog3*$^{EGFP/EGFP}$ plexus with EGFP-reporting cells distributed in reference to the F-actin^{BELT} meshwork at E14.5. Muc1^{+} lumens are dilated, the F-actin^{BELT} meshwork is altered and there is expansion of EGFP^{LO} cells throughout the *Neurog3*$^{EGFP/EGFP}$ plexus. (E-H) *Neurog3*$^{EGFP/+}$ versus *Neurog3*$^{EGFP/EGFP}$ plexus with EGFP-reporting cells in reference to the F-actin^{BELT} meshwork at E17.5. There is high-level activation of the EGFP reporter in the *Neurog3*$^{EGFP/EGFP}$ plexus. (I,J) F-actin^{BELT} shape spectrum from *Neurog3*$^{EGFP/+}$ and *Neurog3*$^{EGFP/EGFP}$ plexus at E14.5 and E17.5. Abnormalities in the E14.5 *Neurog3*$^{EGFP/EGFP}$ plexus are largely corrected by E17.5. I, narrowed F-actin^{BELT}; II, elongated F-actin^{BELT}; III, expanded F-actin^{BELT}; IV, expanded and elongated F-actin^{BELT}. (K) Schematic of the general pattern of F-actin^{BELT} shape change as normal epithelial cells transition from plexus (blue) to duct (orange) or to *Neurog3*-expressing states (red). Green dashed line outlines the F-actin^{BELT} spectrum in *Neurog3*$^{EGFP/EGFP}$ plexus at E14.5. (L) Schematic showing morphological alterations associated with states of *Neurog3* activation (green) in *Neurog3*$^{EGFP/+}$ and *Neurog3*$^{EGFP/EGFP}$ epithelium. Scale bars: 15 µm in A-D, 20 µm in E-H.

represent filopodial migratory activity at the basal leading edge of the cell (Fig. 3C,C′; Fig. S7A) (Bechard et al., 2016; Löf-Öhlin et al., 2017). Progressive basalward movement was associated with elongation of the Muc1^{+}F-actin^{FOCAL} structures, and an eventual detachment from the lumenal surface (Fig. 3D,D′), signifying completion of cell egress from the epithelium. A *Neurog3*^{BAC} transgenic reporter line *Neurog3*^{RG1} (hereafter *Neurog3*^{RG}) (Bechard et al., 2016) independently confirmed the association of apical narrowing, focalization and basalward cell displacement with acquisition of the *Neurog3*^{HI} state (Fig. 3F-I′; Fig. S7B-D′). These results suggest that *Neurog3* upregulation within the plexus occurs concomitantly with a finely resolved sequence of events beginning with apical narrowing, then F-actin^{FOCAL} formation and basalward cell movement during endocrine-cell birth (Fig. 3E,J).

Neurog3-independent and Neurog3-dependent regulation of the endocrine-cell birth process

Although *Neurog3*$^{EGFP/EGFP}$ (null) pancreata lack differentiated endocrine cells (Gradwohl et al., 2000; Shih et al., 2012), the late-stage correctively remodeling *Neurog3*$^{EGFP/EGFP}$ plexus contained many *Neurog3*$^{EGFP-HI}$ cells. To define the stage in endocrine-cell birth when Neurog3-deficient cells fail, we compared the progression of *Neurog3*$^{EGFP/+}$ and *Neurog3*$^{EGFP/EGFP}$ Muc1^{+}EGFP^{+} cells through apical narrowing, F-actin^{FOCAL} formation and basalward movement. In E14.5 *Neurog3*$^{EGFP/EGFP}$ pancreata, cells exhibited a uniformly circular and narrowed apical surface compared with heterozygous controls, with essentially all being EGFP^{LO} (Fig. 3K,M). In the late-stage ‘corrected’ *Neurog3*$^{EGFP/EGFP}$ plexus, however, 58.5% of all Muc1^{+}EGFP^{HI} cells (n=91) were apically narrowed, versus 18.3% in the *Neurog3*$^{EGFP/+}$ plexus (n=82) (Fig. 3K-R), suggesting that *Neurog3*^{NULL} cells do not efficiently progress past apical narrowing (Fig. S8A). The lengths of F-actin^{FOCAL} structures in *Neurog3*-null Muc1^{+}EGFP^{HI} cells were reduced relative to control (Fig. S8C,D), suggesting reduced basalward movement and consistent with indications of diminished protrusive distortions at the basal surface (Fig. S8C-E). Finally, a small proportion of Muc1^{+}EGFP^{HI} *Neurog3*$^{EGFP/EGFP}$ cells were non-apically narrowed and not basally displaced (15.3% of all *Neurog3*$^{EGFP/EGFP}$ Muc1^{+}EGFP^{HI} cells versus 2.3% in *Neurog3*$^{EGFP/+}$ controls;

Development (2018) 145, dev162115. doi:10.1242/dev.162115

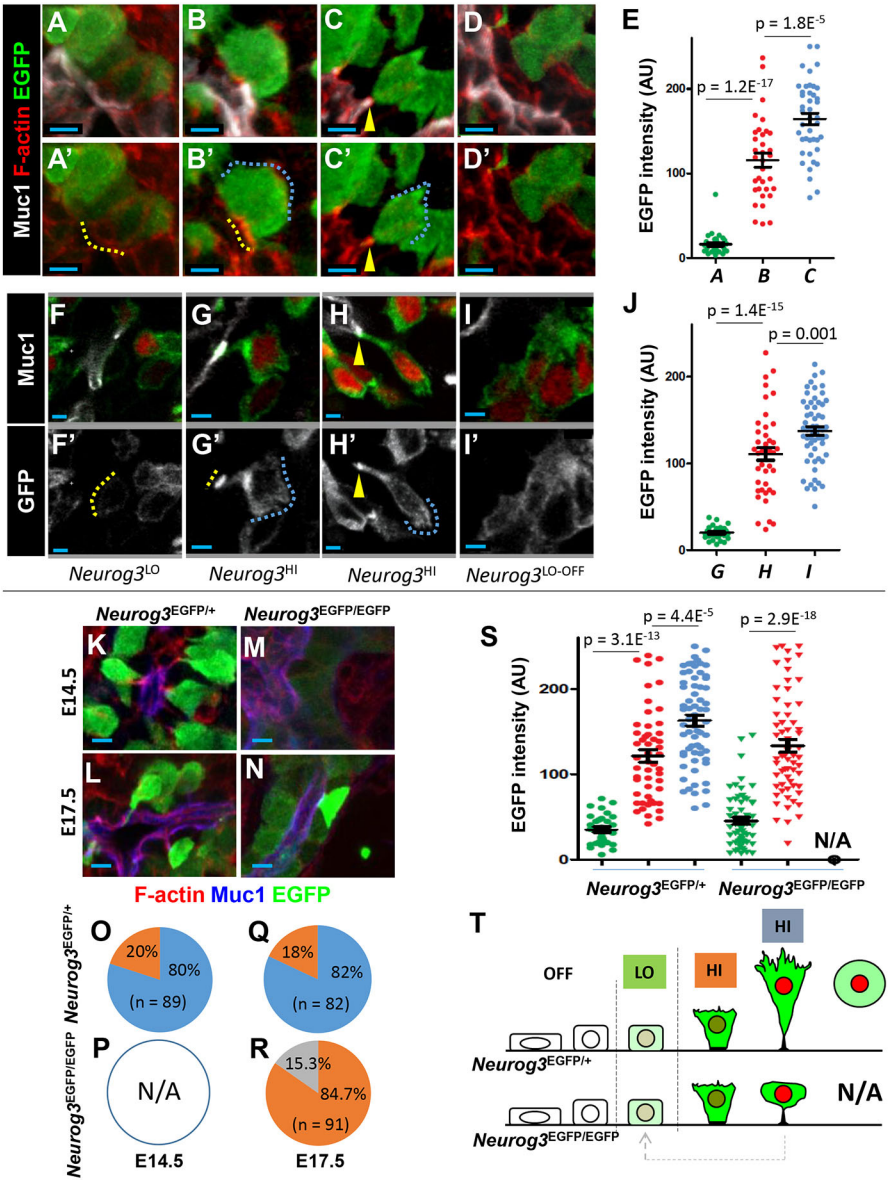

Fig. 3. *Neurog3*-independent apical narrowing and *Neurog3*-dependent basalward cell displacement guide endocrine-cell birth. (A-D′) *Neurog3*$^{EGFP/+}$ EGFP^{+} cells showing step-wise progression from non-apically narrowed and non-egressing EGFP^{LO} to an apically narrowed (yellow dashed line) or F-actin^{FOCAL}-associated basally displaced (blue dashed line) EGFP^{HI} state, and finally to an apically detached state. (E) Mean fluorescence intensity measurements (AU, arbitrary units) in cells non-apically narrowed, apically narrowed or basally displaced. (F-I′) *Neurog3*$^{RG+}$ cells showing similar progression as in A-D′. (K) Mean fluorescence measurements as in E. (K,L) EGFP^{+} cells in *Neurog3*$^{EGFP/+}$ plexus. (M,N) EGFP^{+} cells in *Neurog3*$^{EGFP/EGFP}$ plexus. (O-R) Percentage of Muc1^{+}EGFP^{HI} cells in non-apically narrowed (gray), apically narrowed (orange) and basally displaced (blue) states in each genetic condition. (S) Fluorescence intensities from non-apically narrowed (green), apically narrowed (red) and basally displaced (blue) EGFP^{+} cells in E17.5 *Neurog3*$^{EGFP/+}$ and *Neurog3*$^{EGFP/EGFP}$ epithelium. (T) Schematic showing *Neurog3*-independent and *Neurog3*-dependent steps during *Neurog3* upregulation and cell egression. Scale bars: 5 µm in A-D′,K-N; 3 µm in F-I′.

Fig. 3R-T). We interpret this population as cells that had previously entered the initial stages of apical narrowing, focalization and *Neurog3* upregulation, but then failed in apical-surface detachment and returned to the epithelium. These data show that complete Neurog3 deficiency compromises, but does not completely block, cells in the plexus from entering the sequence of apical narrowing, focalization and basalward movement normally defined by the endocrine-committed *Neurog3*^{HI} state. Moreover, these data suggest that a program of morphogenetic regulation of apical narrowing, focalization and basalward cell movement can be effected independent of Neurog3 protein function (Fig. 3T).

NmMyoII-dependent pathways mediate plexus morphogenesis and endocrine-cell birth

The molecular motor nmMyoII, produced as IIa (Myh9), IIb (Myh10) or IIc (Myh14) isoforms, acts on F-actin substrates to drive processes such as apical constriction and cell delamination (Martin and Goldstein, 2014). The active phosphorylated form of nmMyoII light chain (p-nmMyoII) was detected at the apical aspect of pancreatic epithelial cells, in a pattern consistent with close localization to the F-actin^{BELT} network (Fig. S9A,B). The p-nmMyoII signal was detected on most but not all Muc1^{+} F-actin^{FOCAL} structures (Fig. S9C,D). Immunodetection of nmMyoIIa/IIb isoforms showed a substantial signal in the blood vessels and a lower pan-mesenchymal signal (Fig. S9K,L), consistent with our detecting p-nmMyoII in both tissues (data not shown). The available reagents did not detect nmMyoIIa/IIb in the pancreatic epithelium or in *Neurog3*^{EGFP}-expressing cells. Analysis of nmMyoIIC using a GFP fusion knock-in mouse strain (Ebrahim et al., 2013), however, showed a pattern surprisingly selective for the epithelium at E14.5, which became largely restricted to non-acinar epithelium by E17.5 (Fig. S9E-J), and a low nmMyoIIc-GFP signal in differentiated endocrine cells (data not shown). These data are consistent with roles for nmMyoII activity in mediating epithelial morphogenesis and endocrine differentiation in the plexus.

NmMyoII activity maintains the plexus state and promotes endocrine differentiation

To assess potential function(s) of nmMyoII in apical-surface narrowing and focalization within the plexus, we explanted

Development (2018) 145, dev162115. doi:10.1242/dev.162115

plexus-rich segments of E15.5 dorsal pancreata (Fig. 4A), and cultured them with or without the nmMyoII inhibitor blebbistatin (BBS) (Straight et al., 2003), which directly interferes with intrinsic GTPase motor activity (Kovacs et al., 2004) to inhibit all nmMyoII-dependent processes. With vehicle treatment over 36 h of culture, the plexus maintained gross morphological features similar to those observed at equivalent *in vivo* stages. Conversely, BBS inhibition caused a broad, rapid and reproducible transformation of the plexus into an abnormal 'duct-like' state that exhibited increased lumen diameter and flattened epithelial cell morphologies (Fig. 4B-G). Within these transformed duct-like states, F-actin^{BELT} perimeters became enlarged compared with those in untreated explants (Fig. 4H-L). Much of any remaining plexus exhibited distended lumens that were prominent at the 'nodes' where epithelial segments of the plexus intersected, and acinar lumens were also distended (Fig. S10A-F). The BBS-mediated effects on epithelial morphology were dose dependent and reversible. An 18 h BBS washout led to restoration of normal F-actin^{BELT} morphologies (Fig. S11A-H), indicating a robust recovery in the 25-50 µM dose-range of live tissue with differentiating endocrine cells (not shown). These BBS doses and time frames of exposure that caused minimal cell death in the explants (not shown) were consistent with the notion that the effects on epithelial morphology were likely the outcome of acute nmMyoII inhibition. The effects of BBS on plexus morphology were not caused by loss of epithelial integrity or apical polarity, because aPKC, the primary cilium marker γ-tubulin, and E-cad maintained their respective apical and basolateral localizations during the experimental timeframe (Fig. S12A-F). Concomitant with BBS-induced duct-like transformation, there was a marked decrease in the number of Neurog3^{+} cells (Fig. 4C,F, quantified below). In rare regions where plexus remained, large numbers of both Neurog3^{+} cells still existed, suggesting that BBS had not accessed all areas of the explant volume equivalently, and that in such areas endocrine-cell birth could progress forward. Additionally, although the immunofluorescent signal for Sox9 was somewhat reduced in BBS-treated explants, there was no change in epithelial Pdx1 or Prox1 immunodetection intensity (Fig. S13A-H), suggesting that the reduced Neurog3^{+} cell numbers did not result from loss of pancreatic epithelial identity (Westmoreland et al., 2012). These experiments targeting nmMyoII activity, although not cell-type specific in nature, suggest functions for nmMyoII in limiting apical surface size, in maintaining the plexus morphology and in mediating the production of Neurog3-expressing populations within the plexus (Fig. 4M).

ROCK-nmMyoII activity mediates sequential steps in the delamination of Neurog3-expressing cells

ROCK-nmMyoII pathway activity has been shown to regulate apical narrowing, cell migration and cell-rear retraction (Riento and Ridley, 2003; Worthylake et al., 2001), and our data presented here and that of others (Gouzhi et al., 2011) suggest that these processes are essential for endocrine-cell birth. To test how separate parts of the ROCK-nmMyoII pathway influence epithelial morphogenesis and endocrine-cell birth, we tested whether pharmacological inhibitors of ROCK and nmMyoII block or augment apical narrowing, focalization and basalward cell displacement in *Neurog3*-expressing cells. Consistent with our results above, BBS-treated *Neurog3*^{RG} explants showed reduced numbers of *Neurog3*$^{RG+}$ cells along the distended Muc1^{+} lumens (Fig. 5A-D; Fig. S14A-E; quantified below). Among the *Neurog3*$^{RG+}$ cells

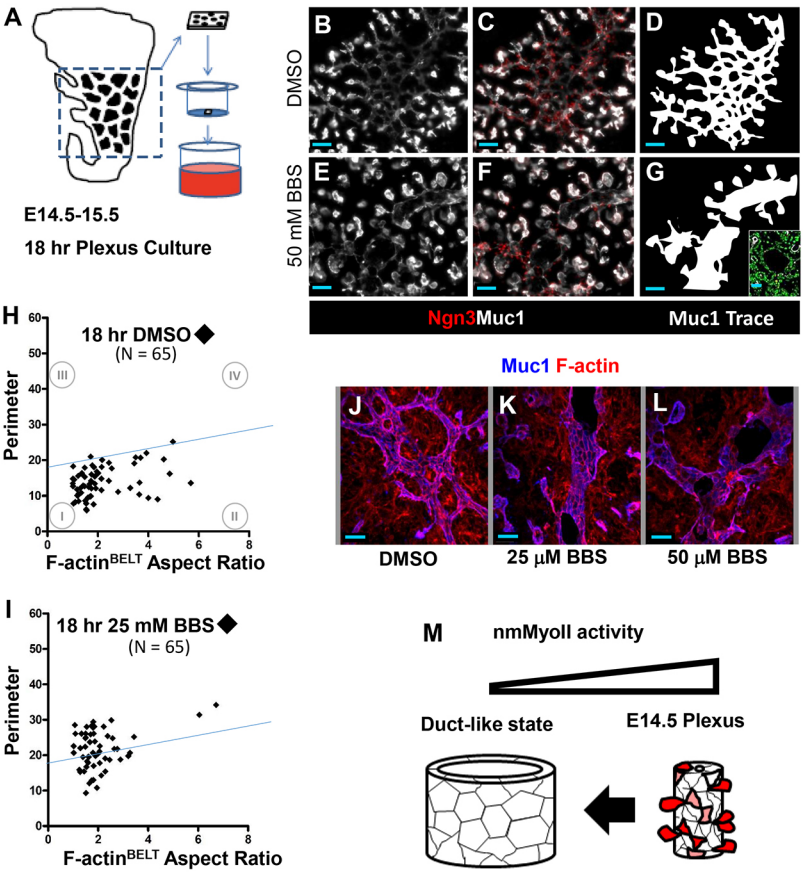

Fig. 4. NmMyoII activity limits apical expansion and promotes generation of Neurog3^{+} cells. (A) Diagram of the culture method. (B-G) Muc1 and Neurog3 immunodetection in explants cultured for 18 h under vehicle or BBS-treated conditions; manual epithelial tracings are shown in D and G. Inset in G shows a sectional plane at higher magnification, with DAPI to indicate position of nuclei related to the Muc1^{+} lumen surface. (H,I) F-actin^{BELT} shapes in explants in vehicle or BBS explants. Blue lines indicate the maximum *y*-axis F-actin^{BELT} dimension measured *in vivo*. I, narrowed F-actin^{BELT}; II, elongated F-actin^{BELT}; III, expanded F-actin^{BELT}; IV, expanded and elongated F-actin^{BELT}. (J-L) Muc1 and F-actin after treatment with increasing BBS doses. (M) Schematic showing the morphological transformation of the plexus into a duct-like state under nmMyoII inhibition. Scale bars: 50 µm in B-G; 30 µm in inset of G; 20 µm in J-L. Data are from *n*=3 explants for each condition.

Development (2018) 145, dev162115. doi:10.1242/dev.162115

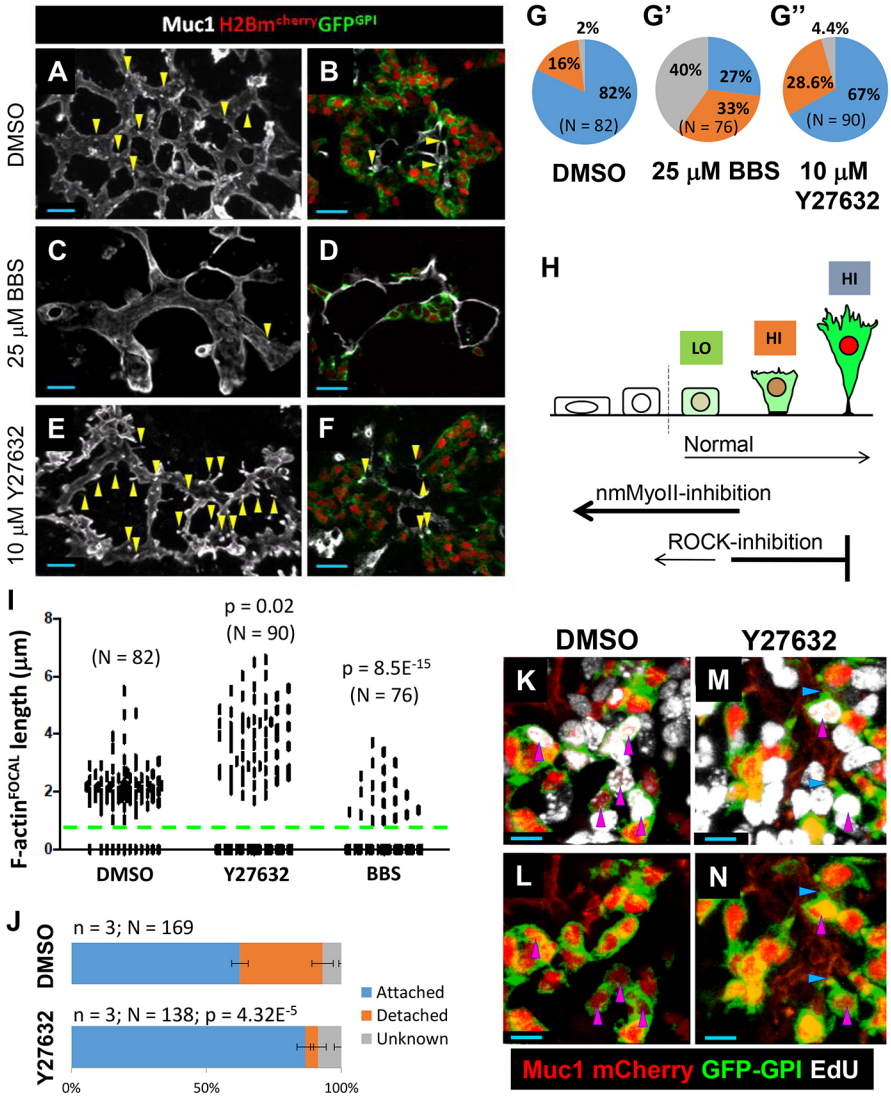

Fig. 5. ROCK-nmMyoII activities mediate morphological transitions during endocrine-cell birth. (A-F) Muc1^{+} and *Neurog3*$^{RG+}$ cells in explants treated with vehicle alone, 25 µm BBS or 10 µM Y27632 for 18 h; Muc1^{+} F-actin^{FOCAL} structures are indicated by yellow arrowheads. There is a reduction in apically narrowed and basally displaced populations after BBS treatment. (G-G″) Proportions of non-narrowed (gray), apically narrowed (orange) and basally displaced (blue) *Neurog3*$^{RG+}$ populations after vehicle, BBS or Y27632 treatment. (H) Schematic showing non-apically narrowed, apically narrowed and basally displaced *Neurog3*-expressing cells in G, and the effect of nmMyoII and ROCK inhibition. (I) Lengths of typical F-actin^{FOCAL} apical tether structures after vehicle, Y27632 or BBS treatment. Green dashed line indicates the distinction between an apically narrowed surface (no F-actin^{FOCAL} length or <1.0 µm) versus an elongated F-actin^{FOCAL} structure (>1.0 µm). (J) EdU pulse-chase quantification of defective cell-rear retraction in Y27632-treated explants. (K-N) EdU^{+} *Neurog3*$^{RG+}$ cells exhibiting attached (blue arrowheads) or detached (pink arrowheads) cell rears. Scale bars: 20 µm in A-F; 5 µm in K-N. Data are from *n*=3 explants for each condition.

present in BBS-treated explants, quantification of non-apically narrowed, apically narrowed and basally displaced *Neurog3*$^{RG+}$ cells indicated a distinct shift toward a non-apically narrowed and non-displaced positioned state (Fig. 5G,G′). The Muc1^{+} F-actin^{FOCAL} structures observed showed a decreased length compared with controls (Fig. 5H,I). These results fit the notion that nmMyoII activity is crucial for apical narrowing, focalization and basalward cell movement during endocrine-cell birth.

Blocking ROCK activity with Y27632 (Uehata et al., 1997) is known to alter cell migration and also cause defects in cell-rear retraction in some cell types, with such changes attributed, at least in part, to ROCK-mediated modulation of nmMyoII activity, actin-filament stabilization and disassembly of integrin-signaling complexes (Riento and Ridley, 2003; Worthylake et al., 2001). In pancreatic explants, ROCK inhibition led to several effects on tissue and cell morphology that were noticeably distinct from those under nmMyoII inhibition. Y27632-treated explants showed no evidence of plexus transformation into ‘duct-like’ states, and there was no decrease in the number of Muc1^{+} *Neurog3*$^{RG+}$ cells exiting from the epithelium (Fig. 5E-G,G″). Upon close inspection, and consistent with known functions for ROCK in regulating cell migration, reporter-positive *Neurog3*$^{RG+}$ cells (we did not specifically distinguish between reporter-high versus low states in these drug-treatment conditions) scored in Y27632-treated explants displayed increased basalward movement relative to control *Neurog3*$^{RG+}$ cells (Fig. S14A,F-I). Treatment with Y27632 increased the number of *Neurog3*$^{RG+}$ cells with, as well as length of, F-actin^{FOCAL} structures at their apical surface (Fig. 5E,F,I) suggesting a block in detachment of the apical-cell rear, even with the exaggerated basalward movement of these cells. We confirmed a cell-rear detachment defect in *Neurog3*$^{RG+}$ cells using EdU pulse-chase methods. Briefly, replicating progenitor cells incorporate EdU at S phase, and over a 17-24 h period a proportion of them differentiate and become epithelially detached (Muc1^{-}) (Bankaitis et al., 2015). Defective rear detachment caused by Y27632 treatment should thus cause an accumulation of EdU^{+} Muc1^{+} *Neurog3*$^{RG+}$ cells. One hour after EdU injection into pregnant dams, E13.5 pancreas was explanted and cultured for 18 h with or without Y27632. Confocal *z*-stack volumes of EdU pulse-labeled explants were scored for attached (Muc1^{+}) or detached (Muc1^{-}) EdU^{+} *Neurog3*$^{RG+}$ states. In vehicle controls, 63.4±3.1% of EdU^{+} *Neurog3*$^{RG+}$ cells were Muc1^{+}, 30.6±3.9% were Muc1^{-} and 7.0±1.0% were non-categorizable (Fig. 5J-L). In Y27632-treated explants, 86.6±3.1% of EdU^{+} *Neurog3*$^{RG+}$ cells were Muc1^{+}, 4.8±2.9% Muc1^{-} and 8.6±2.7% were non-categorizable (Fig. 5J,M,N). These data are consistent with two functions for ROCK in the birth of endocrine

Development (2018) 145, dev162115. doi:10.1242/dev.162115

cells: first in limiting basalward movement, and then in directing cell-rear detachment to allow epithelial exit. Finally, short-term (6 h) time-lapse videos of pancreatic explants cultured on fibronectin, with or without BBS or Y27632, confirmed that nmMyoII inhibition reduced, whereas ROCK inhibition augmented, basalward movement of *Neurog3*$^{RG+}$ cells (Fig. S15A-O). Thus, ROCK and nmMyoII coordinate different aspects of endocrine-cell delamination by regulating apical narrowing, focalization, basalward movement and detachment of the rear of the cell from its focalized apical contact.

nmMyoII activity is necessary for Neurog3 activation in the absence of Notch-mediated repression

Because nmMyoII inhibition blocked behaviors associated with endocrine commitment and reduced the numbers of Neurog3^{+} cells, we hypothesized that nmMyoII activity is required for acquisition of the Neurog3-expressing state. We therefore quantified how BBS affected the number of Muc1^{+}Neurog3^{+} cells formed in explants, as a metric for the BBS effect on all *Neurog3*-expressing states. Notably, because the processes of apical narrowing and focalization were perturbed under BBS-treated conditions, we lacked key criteria necessary for quantifying changes in the numbers of *Neurog3*^{LO} versus *Neurog3*^{HI} cells, and thus do not report on such changes here. Comparison of the (Neurog3^{+}Muc1^{+}DAPI^{+})/(Neurog3-negative Muc1^{+}DAPI^{+}) cell fraction in E15.5 explants treated with BBS or vehicle showed a near 50% reduction in all Neurog3^{+} cells under nmMyoII inhibition (Fig. 6A-B′,E). We next tested the effect of nmMyoII inhibition in the presence or absence of the small-molecule Notch inhibitor DBZ (Milano et al., 2004), which causes 'default' derepression of *Neurog3* and acquisition of the Neurog3^{+} state (Serup, 2012; Bankaitis et al., 2015). Consistent with this effect, DBZ-only explants showed ∼2.5-fold increase in total (Neurog3^{+}Muc1^{+}DAPI^{+})/(Neurog3-negative Muc1^{+}DAPI^{+}) cells over vehicle alone (Fig. 6C,C′,E). In BBS/DBZ-treated explants, Neurog3^{+} cell numbers increased slightly over vehicle alone, but were greatly reduced compared with DBZ alone (Fig. 6D-E). These results indicate that nmMyoII inhibition interferes with processes controlling *Neurog3* transcriptional activation or upregulation, or both, even when in the context of induced escape from Notch repression, suggesting that endocrine-cell birth requires permissive inputs supplied by nmMyoII activity.

ROCK activity suppresses the Neurog3^{LO-HI} transition

Apical focalization and initiation of basalward movement are associated with the *Neurog3*^{HI} state in normal and *Neurog3*-null epithelium (Fig. 3). Because ROCK inhibition augmented apical

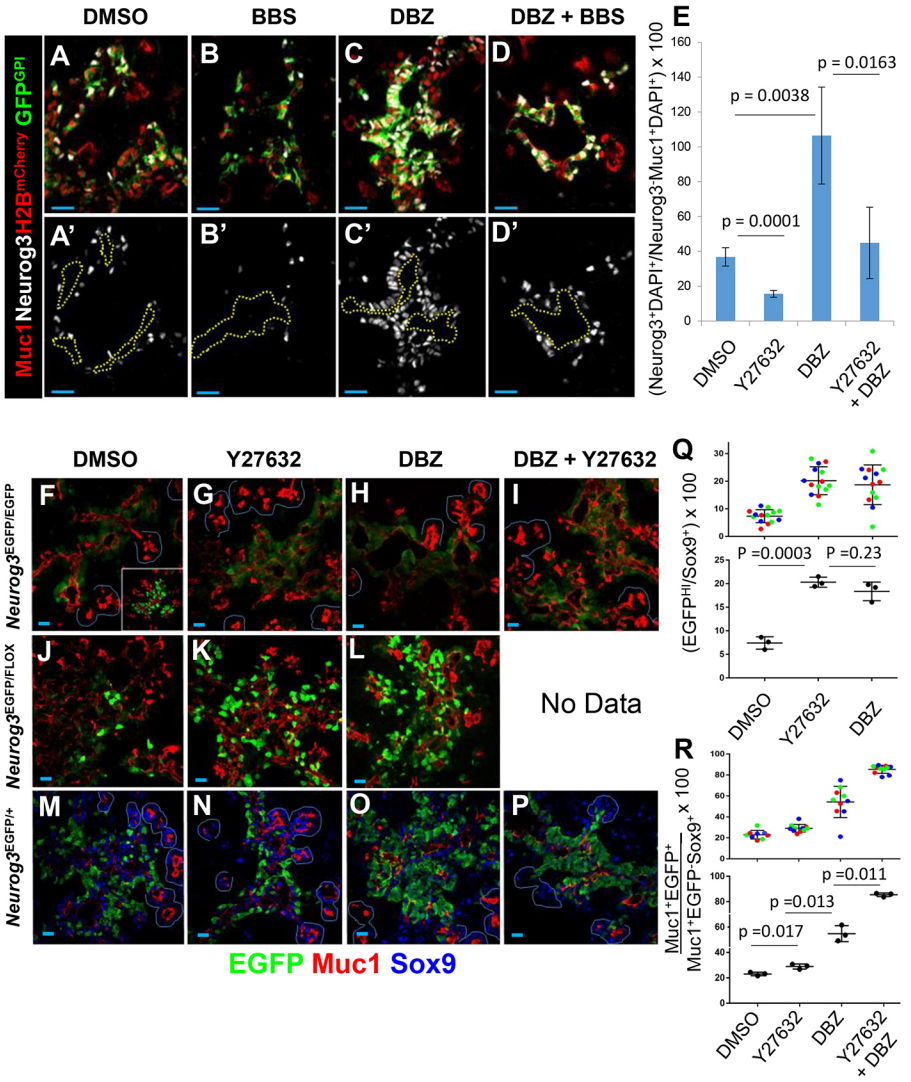

Fig. 6. ROCK-nmMyoII, Notch and *Neurog3* gene dosage regulate acquisition of *Neurog3*-expressing states. (A-D′) Muc1 and Neurog3 protein in E15.5 *Neurog3*$^{RG+}$ explants after treatment with vehicle alone, 25 µM BBS, 20 nM DBZ, or BBS and DBZ. BBS was applied for 18 h with DBZ added 6 h into culture (DBZ exposure, 12 h). (E) Numbers of Muc1^{+} DAPI^{+} cells that are Neurog3^{+} in each condition (DAPI^{+} signal not shown). (F-I) Muc1, EGFP and nuclear Sox9 (latter not shown) in E13.5 *Neurog3*$^{EGFP/EGFP}$ explants treated with 10 µM Y27632, 20 nM DBZ or Y27632 plus DBZ for 18 h. (J-L) E13.5 *Neurog3*$^{EGFP/Flox}$ explants treated and analyzed according to F-H. (M-P) Muc1, EGFP and Sox9 in E13.5 *Neurog3*$^{EGFP/+}$ explants treated according to F-I. (Q) Quantification of endocrine-committed EGFP^{HI} Sox9^{-} cells compared with Sox9^{+} cells in 40× *z*-stacks (∼20 µm) *Neurog3*$^{EGFP/Flox}$ hypomorph explants treated with vehicle, Y27632 or DBZ. Upper colored panel shows spread of raw data, each dot representing one *z*-stack and each color representing an individual biological replicate (mean±s.d.). (R) Quantification of total (Muc1^{+}EGFP^{+})/(total Muc1^{+}EGFP^{-}Sox9^{+}) cells in *Neurog3*$^{EGFP/+}$ explants treated with vehicle, Y27632, DBZ, or DBZ and Y27632. Upper colored panel shows data represented as in Q (mean±s.d.). Scale bars: 20 µm for A-D′; 10 µm for F-P. Blue lines indicate acinar clusters. $n \geq 3$ pancreata for each condition. For E, Q and R, $n=3$ pancreata for each condition; significance is determined using Student's *t*-test.

Development (2018) 145, dev162115. doi:10.1242/dev.162115

focalization and basalward movement in *Neurog3*-expressing cells (Fig. 5), we hypothesized that ROCK normally functions to limit endocrine-cell birth. We first tested whether Y27632 treatment can alleviate the defective *Neurog3* transcriptional upregulation observed in early-stage *Neurog3*$^{EGFP/EGFP}$ (null) explants. In *Neurog3*$^{EGFP/EGFP}$ explants, *Neurog3* is broadly activated at low levels, but Y27632 did not increase the number of *Neurog3*^{HI} cells (Fig. 6F,G). Thus, Y27632 treatment is not able to promote *Neurog3* upregulation in the absence of Neurog3 protein function. We next tested whether ROCK inhibition could raise the level of *Neurog3* expression in cells already expressing low levels of functional Neurog3 protein, by exposing explants from a strong hypomorphic condition, *Neurog3*$^{EGFP/Flox}$ (Wang et al., 2010), to Y27632. *Neurog3* hypomorphs are much more prone to maintaining cells in the *Neurog3*^{LO} state than are wild-type or heterozygous-null controls in which most cells progress forward to the *Neurog3*^{HI} state (Wang et al., 2010; Bechard et al., 2016). Accordingly, vehicle-treated *Neurog3*$^{EGFP/Flox}$ tissues had significantly increased Muc1^{+}Sox9^{+}EGFP^{LO} cell numbers over vehicle-treated *Neurog3*$^{EGFP/+}$ explants, and much reduced numbers of endocrine-committed Muc1^{+}Sox9^{-}EGFP^{HI} cells (Fig. 6J versus M). The Y27632-treated *Neurog3*$^{EGFP/Flox}$ explants, however, showed near-complete restoration of Muc1^{+}Sox9^{-}EGFP^{HI} numbers towards those seen in vehicle-treated *Neurog3*$^{EGFP/+}$ and in 20 nM DBZ-treated *Neurog3*$^{EGFP/Flox}$ explants (Fig. 6K-Q). Therefore, we conclude that ROCK activity normally gates the transition from *Neurog3*^{LO} to *Neurog3*^{HI} states, and ROCK inhibition can bypass the defects in *Neurog3* upregulation seen under *Neurog3* hypomorphism. Interestingly, Y27632-treated *Neurog3*$^{EGFP/+}$ explants exhibited only a slight increase in the total Muc1^{+}EGFP^{+}/Muc1^{+}EGFP^{-}Sox9^{+} cell number relative to vehicle, indicating that Y27632 does not cause augmentation of *Neurog3* activation or upregulation when a normal number of Neurog3-expressing cells are present (Fig. 6M,N,R).

Notch and ROCK suppress endocrine differentiation through distinct mechanisms

That ROCK inhibition does not substantially increase *Neurog3*^{HI} cell numbers in *Neurog3*$^{EGFP/+}$ explants, but does in *Neurog3* hypomorphs (Fig. 6Q,R), implies that ROCK inhibition cannot promote *Neurog3*^{HI} cell numbers if large numbers of *Neurog3*^{HI} cells are already present. We proposed that this inability resulted from Notch-mediated lateral inhibition from the *Neurog3*^{HI} cell population. To test this idea, we treated heterozygous *Neurog3*$^{EGFP/+}$ explants with DBZ and Y27632 together, and compared total cell numbers (Muc1^{+}EGFP^{+}/Muc1^{+}EGFP^{-}Sox9^{+}) with those after vehicle, Y27632 or DBZ treatment. DBZ/Y27632 co-treated *Neurog3*$^{EGFP/+}$ explants showed a large increase in total (Muc1^{+}EGFP^{+}/Muc1^{+}EGFP^{-}Sox9^{+}) cells over DBZ or Y27632 alone (Fig. 6M-P,R). These data suggest that the failure of Y27632 to promote robust *Neurog3* upregulation in *Neurog3*$^{EGFP/+}$ explants is circumvented by inhibiting Notch activity, and thus that ROCK inhibition stimulates *Neurog3* activation and upregulation provided that cells escape Notch repression. Notably, the majority of Muc1^{+}EGFP^{+} cells in DBZ-treated *Neurog3*$^{EGFP/+}$ explants remained Sox9^{+} (Fig. S16B), suggesting that pharmacological Notch inhibition derepresses *Neurog3* expression but interferes with the normal process of *Sox9* downregulation normally associated with *Neurog3* upregulation (Shih et al., 2012). Because this effect is not seen in the context of Y27632 alone, we propose it likely that ROCK and Notch activity regulate endocrine differentiation through separate mechanisms or at different stages of Neurog3 activation and upregulation. Like Y27632 alone, DBZ alone had no apparent effect on the number of cells upregulating EGFP-reporter in homozygous null explants, nor did DBZ and Y27632 in combination (Fig. 6F-I), indicating that the ability of DBZ or Y27632, both individually and in combination, to cause *Neurog3* upregulation is dependent on the presence of at least low levels of Neurog3 protein. These results suggest that, provided Neurog3 protein is available, ROCK activity limits the normal transition of *Neurog3*^{LO} cells to *Neurog3*^{HI} endocrine-committed cells.

Large-scale compensatory synergy between morphogenetic and endocrine-birth programs under reduced Neurog3 function

The results presented above, together with evidence from other reports, suggest that *Neurog3* gene dose, Notch and ROCK-nmMyoII work together in a feedback control circuit that coordinates endocrine fat allocation, progenitor growth and epithelial plexus morphogenesis (Wang et al., 2010; Magenheim et al., 2011; Bankaitis et al., 2015). We were interested in the degree of robustness of this circuit, and its ability to yield, under various degrees of challenge, compensatory functions in driving the linked processes of morphogenesis and endocrine differentiation. We reasoned that the late-stage corrective remodeling of an initially (E14.5) abnormal *Neurog3*$^{EGFP/EGFP}$ plexus, occurring concurrent with a partial restoration of *Neurog3*^{HI} cell number (Fig. 2), reflects the presence but only partial success of a compensatory response. We proposed that the failure to fully restore *Neurog3*^{HI} cell numbers resulted from the absence of feedback signals normally derived from endocrine-committed Neurog3 protein-producing cells during their departure from the plexus epithelium. We therefore tested whether a hypomorphic level of Neurog3 represented a sufficient feedback stimulus to confer a full compensatory response linking conversion of the plexus into an epithelial structure with a full restoration of Neurog3^{HI} endocrine-committing cells. We quantified the number of apically narrowed Muc1^{+}EGFP^{HI} cells in the plexus (Muc1^{+}EGFP^{HI} cells as a proportion of Sox9^{+} cells) at E13.5, E16.5 and E18.5 to compare endocrine-cell birth as a function of plexus remodeling in *Neurog3*$^{EGFP/+}$, *Neurog3*$^{EGFP/Flox}$ and *Neurog3*$^{EGFP/EGFP}$ states. *Neurog3*$^{EGFP/+}$ pancreata showed robust endocrine differentiation in all E13.5, E16.5 and E18.5 samples. The *Neurog3*$^{EGFP/EGFP}$-null pancreata again showed that the early and pervasive defects in *Neurog3* upregulation were progressively but only partially rescued by E16.5 and E18.5, confirming that Neurog3-dependent processes induce the normal rate of *Neurog3*^{HI} cell birth (Fig. 7A-F). In the *Neurog3*$^{EGFP/Flox}$ hypomorph, remarkably, although very low numbers existed at early stages, there was a complete restoration of the number of *Neurog3*^{HI} cells by E18.5 (Fig. 7A-J). Thus, even a strongly reduced level of Neurog3 is sufficient to engage, albeit late, an adaptive feedback control circuit that links endocrine differentiation and plexus morphogenesis to establish and maintain the balance between cell differentiation and epithelial remodeling.

DISCUSSION

Our results focus on a new ‘global’ understanding of the functional integration between programs of *Neurog3*-driven endocrine-fate determination, Notch-mediated progenitor maintenance, and ROCK/nmMyoII-mediated epithelial morphogenesis. We describe distinct ways in which the ROCK/nmMyoII pathway mediate a dissociable sequence of epithelial egression events linked to the acquisition of pre-endocrine-committed and endocrine-committed *Neurog3*-expressing states within the dynamically remodeling

Development (2018) 145, dev162115. doi:10.1242/dev.162115

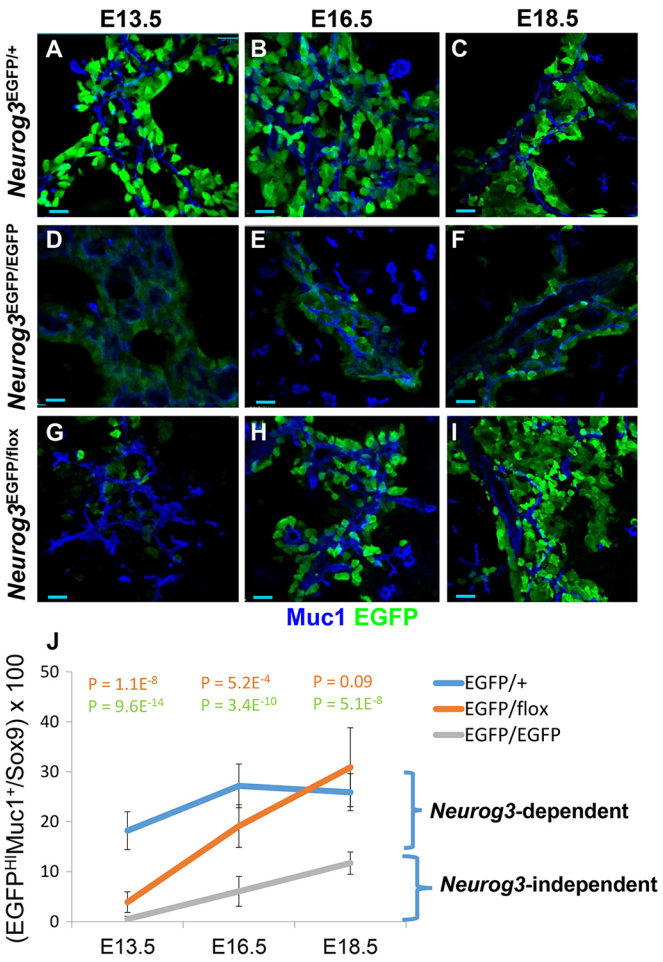

Fig. 7. Plexus morphogenesis intercommunicated with *Neurog3* gene dose drives robust endocrine differentiation. (A-I) Muc1 and EGFP shown as a time-course for plexus remodeling in sectioned (30 µm) *Neurog3*$^{EGFP/+}$ (A-C), *Neurog3*$^{EGFP/EGFP}$ (D-F) and *Neurog3*$^{EGFP/Flox}$ (G-I) pancreata. (J) Quantification of the amount of delaminating endocrine committed (EGFP^{+}Muc1^{+}Sox9^{-} cells)/(total Sox9^{+}EGFP^{-} cells) at each stage. Scoring from images of plexus epithelium was averaged from *n*=3 pancreata (*Neurog3*$^{EGFP/+}$=11, 10 and 9 images for E13.5, E16.5 and E18.5, respectively; *Neurog3*$^{EGFP/EGFP}$=12, 10 and 9 images for E13.5, E16.5 and E18.5, respectively; *Neurog3*$^{EGFP/Flox}$=9, 11, and 14 images for E13.5, E16.5 and E18.5, respectively). Error bars are s.e.m. Scale bars: 15 µm.

epithelium. The main findings of this paper are presented schematically in Fig. S17. We propose that a feedback circuit comprising ROCK/nmMyoII, Notch and Neurog3-dependent influences bestows self-organizing feedback properties that ensure the correct balance between progenitor growth, differentiation and morphogenesis.

Morphogenetic determinants mediate endocrine cell-fate acquisition in plexus progenitors

ROCK/nmMyoII-dependent processes mediate a step-wise cell-egression sequence for progression into and through *Neurog3*^{LO} and *Neurog3*^{HI} states. Inhibiting nmMyoII activity interferes with apical narrowing and focalization, and basalward cell movement, and limits formation of Neurog3^{+} cells. Similar deficits in nmMyoII-inhibited explants occurred even when endocrine cells were overproduced when lifting Notch-mediated repression. Because our experiments did not discern cell-autonomous effects of nmMyoII inhibition, future dissection of its function specifically within *Neurog3*-expressing cells will likely be informative. ROCK inhibition augmented apical narrowing, focalization and basalward cell movement, and efficiently promoted progression of *Neurog3*^{LO} into *Neurog3*^{HI} cells in *Neurog3* hypomorphs, but not in heterozygous *Neurog3*$^{EGFP/+}$ explants with much more robust Notch-mediated inhibition. A pro-endocrine modulation by ROCK inhibition occurred in heterozygous explants only with Notch co-inhibition, implying that, in normal tissue, ROCK de-repression promotes *Neurog3*$^{LO\text{-}to\text{-}HI}$ transitions up to a 'set point' where an appropriate number of *Neurog3*^{HI} cells exert lateral inhibition as a dominant patterning determinant. Thus, we suggest that ROCK and nmMyoII are important factors in mediating timely and spatially localized cellular responses to signals that both drive (Neurog3 as a cell-autonomous instructor) and inhibit (via Notch) endocrine-fate acquisition. Intimate connections between epithelial morphogenesis programs and intrinsic cell-fate gene-regulatory networks are supported by additional studies, such as when Cdc42 inactivation led to failed progenitor-cell apicobasal polarization, block of epithelial tubulogenesis and severe endocrine-cell depletion (Kesavan et al., 2009). This phenotype resulted at least in part from improper positioning of cells within environments conducive for endocrine differentiation, as discussed below. Moreover, perturbation in Pdx1^{+} epithelial cells of CELSR proteins, components of the Wnt/PCP (planar cell polarity) signaling orthogonal to apico-basal polarity, caused large reductions in Neurog3^{+} cells (Cortijo et al., 2012). Other reports connect morphogenesis and differentiation via RhoA (Petzold et al., 2013; Azizoglu et al., 2017) and Rac signaling (Löf-Öhlin et al., 2017). An important link between Rac, apical domain size control and endocrine cell-fate acquisition occurs in mice and humans (Löf-Öhlin et al., 2017). It will be important in the future to dissect how morphogenetic pathways mediate recognition and processing of epithelial cues, possibly under precise local spatial control, that control progenitor growth and cell fate. Targeting such activities could alter the growth and differentiation properties of pancreas-differentiated iPS/ES cells *in vitro*.

Morphogenetic behavior of endocrine-biased progenitors in an asymmetric niche

Stem-cell niche microenvironments are commonly asymmetric, e.g. showing pro-maintenance or pro-differentiation cues at basal or apical aspects of a cell or tissue (Li and Xie, 2005). Theoretically, controlling the timing and exposure to such separated cues could regulate which cells undergo cell-fate allocation, and when. Particularly relevant, therefore, are the associations drawn here, in both *Neurog3*$^{EGFP/+}$ and *Neurog3*$^{EGFP/EGFP}$ pancreata, between apical surface size/shape, basalward cell movement within and away from the epithelium, and *Neurog3* expression. Cells in all genetic conditions studied here, including the Neurog3 protein null, only underwent *Neurog3* upregulation upon narrowing and focalization of their apical surface (F-actin^{FOCAL}) and basalward cell displacement. We suggest, therefore, that apical-basal cell-body positioning within the epithelial plane controls, at least in part, acquisition of distinct *Neurog3*-expressing states upstream of Neurog3 protein function. This finding seems conceptually aligned with zebrafish retinal cell behavior, wherein neurogenesis is coupled to interkinetic nuclear migration along an apical-to-basal Notch gradient (Del Bene et al., 2008). In addition, in the zebrafish retina, apical domain size has been linked to modulation of Notch signaling (Clark et al., 2012). In the fish and mouse pancreas, high, medium and low Notch signaling impart duct, bipotent progenitor and endocrine fates, respectively (Ninov et al., 2012; Shih et al.,

Development (2018) 145, dev162115. doi:10.1242/dev.162115

2012), associated in our studies with large, intermediate or narrowed/focalized apical surfaces. Because ROCK and nmMyoII inhibition showed opposite effects on the derivation of Neurog3^{+} cells, in the presence and absence of Notch inhibition, we suspect that regulation of apical surface size and basalward cell movement is a fundamental function by which ROCK and nmMyoII mediate cell fates.

Transcriptional determinants of cell fate regulate tissue and cellular morphogenesis

Collectively, our data support previous studies suggesting that differentiating endocrine-cell progeny perform a 'feedback support role' for the epithelial plexus niche, and extend the range of functions for Neurog3 beyond its roles as an endocrine-lineage determinant and initiator of Notch-mediated lateral inhibition. The picture emerging is that Neurog3 influences numerous developmental processes in the plexus niche, including driving robust progenitor replication (Bankaitis et al., 2015), non-cell-autonomously refining gene-expression patterning (Wang et al., 2010; Bechard et al., 2016), cell-autonomously determining endocrine-cell fate (Gradwohl et al., 2000; Gu et al., 2002) and regulating tissue morphogenesis (Magenheim et al., 2011; Bankaitis et al., 2015). We show the first evidence that Neurog3-dependent non-autonomous mechanisms stimulate the production of new endocrine cells from the plexus (Fig. 7). We propose that a feedback function for Neurog3^{+} cells drives, or is a strong supportive influence in, the systematic integrative sustenance of epithelial growth and morphogenesis that is balanced with the apportionment of duct versus endocrine cell types. Future analyses might lead to understanding how transcription-factor determinants feed into the morphogenetic programs to build precise micro-environments, and their coordination to ensure timely placement of the right types and numbers of lineages throughout organogenesis. Under Pdx1 deficiency, early dorsal pancreatic bud evagination, cell polarization and microlumen formation all occur (Marty-Santos and Cleaver, 2016; Villasenor et al., 2010) but there is a complete failure in subsequent plexus assembly. Moreover, tissue-specific inactivation of transcription factors – such as HNF1b (De Vas et al., 2015), HNF6 (Pierreux et al., 2006) or Prox1 (Wang et al., 2005; Westmoreland et al., 2012) – all cause epithelial malformations concurrent with defective endocrine lineage allocation. Although these phenotypes were attributed largely to direct effects on genes such as *Neurog3*, equally consistent is the idea that an altered epithelial architecture precludes efficient spatial deployment of signals that drive endocrine differentiation and epithelial morphogenesis programs. Building systems-like network models linking epithelial morphogenesis, gene transcription and intracellular signaling as principal components for a larger 'niche-framework' will be important.

Adaptive self-organization in the plexus niche

We propose that cooperative engagement of adaptive morphogenetic regulation with Neurog3-dependent processes confers robustness on endocrine differentiation, affording resilience even when genetic insults cripple endocrine differentiation (Bankaitis et al., 2015; Fig. 7). In the case of *Neurog3*$^{EGFP/EGFP}$-null epithelium, that the morphologically abnormal plexus state is populated very broadly with *Neurog3*^{LO} cells indicates that signals triggering *Neurog3* transcriptional activation and specifying the endocrine-biased state are extensive over the epithelium. That adaptive restoration of *Neurog3*^{HI} cells occurs only during late-stage 'corrective remodeling' (in association with a specific sequence of cell-shape changes) suggests that localized morphological alterations in the plexus epithelium exert central control over endocrine commitment via *Neurog3* upregulation. Importantly, the restoration of *Neurog3*^{HI} cells is only moderate in the absence of Neurog3 protein (Fig. 7), which we interpret as indicating that plexus morphogenesis normally synergizes with Neurog3-dependent processes to instruct appropriate numbers of endocrine cells to begin exit from the growing, dynamically remodeling epithelium. For example, even with a low level of Neurog3 protein function, the strongly hypomorphic epithelium could essentially completely restore *Neurog3*^{HI} cell numbers back from the massive mid-gestation reduction. We feel that such cross-regulatory feedback between non-autonomous morphogenetic determinants and *Neurog3* represents a large-scale 'community effect' (Gurdon, 1988) to modulate progenitor flux toward the various epithelially derived lineages. We propose that such a community effect is likely influenced by biomechanical (e.g. intra/intercellular tension) and biochemical factors (Cebola et al., 2015; Marinari et al., 2012), some derived directly from endocrine cells engaged in a prolonged process of epithelial egression. Because cell departure is associated with fate acquisition in developing systems across phyla, linking this process to the architecture and behavior of the parental epithelium could reflect a broad process of organ-system self-organization.

MATERIALS AND METHODS

Mice

Neurog3^{EGFP} [B6.129.S-*Neurog3*$^{tm1(EGFP)Khk/Mmcd}$] knock-in (Lee et al., 2001) and *Neurog3*^{FLOX} [*Neurog3*$^{tm1(cre/ERT)Ggu}$] mice (Wang et al., 2008) were from Guoqiang Gu (Vanderbilt University, Nashville, TN, USA). *Neurog3*$^{EGFP/+}$ and *Neurog3*$^{EGFP/EGFP}$ pancreata were assigned definitively via EGFP-fluorescence level and lack of EGFP^{+} islet clusters, all readily observable under epifluorescence and agreeing with PCR genotyping and immunolabeling confirmation of genotype, as expected for a coding-region deletion allele. Tables S1 and S2 describe *Neurog3*$^{EGFP/EGFP}$ and *Neurog3*$^{Flox/+}$ genotyping, and *Neurog3*$^{EGFP/Flox}$ PCR genotyping followed Wang et al. (2010). *Neurog3*^{RG1} mice were genotyped as described (Bechard et al., 2016). nmMyoIIC^{GFP} mice were a kind gift from Robert Adelstein (National Heart, Lung, and Blood Institute, Bethesda, MD, USA). Wild-type mice were of mixed genetic background. All protocols were approved by Vanderbilt University IACUC.

Immunofluorescence analysis

Embryonic pancreas was fixed in paraformaldehyde (4%, 4°C for 4-6 h, Fisher 04042-500) and for cryosectioning was sucrose equilibrated (30%, 4° C overnight, VWR 0335-12KG) and embedded in OCT (Tissue-Tek, Sakura). A Leica CM3050 S produced thick sections of 30-40 µm or 10 µm thin sections. Table S1 lists primary antibodies incubated overnight at 4°C in PBS containing 0.1% Triton X100, 0.5% BSA and 0.01% sodium deoxycholate. All secondary antibodies were from Jackson ImmunoResearch Laboratories, used at 1:500. Imaging was carried out using a Zeiss Apotome or confocal Zeiss LSM 510 META microscope. Confocal *z*-stack volumes were acquired at 40× magnification with 3D reconstructions using Imaris software. To measure apical F-actin cortices, 2D sections (1.5-2.0 µm sectional planes) from 3D volumes were assessed for whole F-actin^{BELTS} visible along the Muc1^{+} lumen surface, perimeter: aspect ratio was determined by line or polygon-trace functions in Imaris.

Quantification and statistical analyses

Distinguishing plexus and non-plexus states was carried out as described (Bankaitis et al., 2015). Fluorescence intensity measurements used mean pixel intensity in ImageJ. Sox9 and Neurog3 numbers were counted manually. For Neurog3^{+} or EGFP^{+} explant analysis, cell numbers in each state were summed from individual plexus volumes (six or more for each sample, ~30% of total explant), averaged within each sample, and averaged between all samples. Measurements of morphological structures and nuclear

Development (2018) 145, dev162115. doi:10.1242/dev.162115

densities were made using line or polygon-trace functions in Imaris. Nuclei were defined by H2B-mCherry signal in *Neurog3*^{RG} samples or Sox9 immunopositivity in *Neurog3*$^{EGFP/+}$ and *Neurog3*$^{EGFP/EGFP}$ samples. Low-level Sox9 immunopositivity in cells initiating epithelial egression in *Neurog3*$^{EGFP/+}$ samples was digitally enhanced (brightness and contrast) in Image J. All Student's *t*-tests were two-tailed.

Drug treatments

Explants were cultured at 37°C in 5% CO_2 at the air-liquid interface on trans-well supports (Costar 3422) in DMEM (no phenol red) with 10% FBS, penicillin/streptomycin (10 U/ml each) and 1% L-glutamine (Shih and Sander, 2014). Blebbistatin [Abcam, S(-) form, CAS, 856925-71-8], Y27632 (Selleckchem, S1049) and DBZ (Cayman Chemical, 209984-56-4) or vehicle (0.1% DMSO final) were added. Explants were fixed (for 2 h in 4% paraformaldehyde) for analysis.

Acknowledgements

We thank Drs Matt Tyska, Roland Stein and Guoqiang Gu (Vanderbilt University), and various Gu and Wright lab members for helpful discussions. Supporting data were gathered in the Vanderbilt Cell Imaging Shared Resource using imaging scholarships from the Vanderbilt University Medical Center Digestive Disease Research Center and Diabetes Research and Training Center and the Vanderbilt-Ingram Cancer Center, supported by the National Institutes of Health.

Competing interests

The authors declare no competing or financial interests.

Author contributions

Conceptualization: E.D.B., M.E.B., G.G., M.A.M., C.V.E.W.; Methodology: E.D.B., M.E.B.; Software: E.D.B.; Validation: E.D.B., C.V.E.W.; Formal analysis: E.D.B.; Investigation: E.D.B., M.E.B., C.V.E.W.; Resources: G.G., M.A.M., C.V.E.W.; Data curation: E.D.B.; Writing - original draft: E.D.B., C.V.E.W.; Writing - review & editing: E.D.B., M.E.B., C.V.E.W.; Visualization: E.D.B.; Supervision: G.G., C.V.E.W.; Project administration: C.V.E.W.; Funding acquisition: C.V.E.W.

Funding

Project funding was from the National Institutes of Health (1UO1DK089570-01). Deposited in PMC for release after 12 months.

Supplementary information

Supplementary information available online at
http://dev.biologists.org/lookup/doi/10.1242/dev.162115.supplemental

References

Afelik, S., Qu, X., Hasrouni, E., Bukys, M., Deering, T., Nieuwoudt, S., Rogers, W., MacDonald, R. and Jensen, J. (2012). Notch-mediated patterning and cell fate allocation of pancreatic progenitor cells. *Development* **139**, 1744-1753.

Amano, M., Nakayama, M. and Kaibuchi, K. (2010). Rho-Kinase/ROCK: a key regulator of the cytoskeleton and cell polarity. *Cytoskeleton* **67**, 545-554.

Apelqvist, A., Hao, H., Sommer, L., Beatus, P., Anderson, D. J., Honjo, T., Hrabe de Angelis, M., Lendahl, U. and Edlund, H. (1999). Notch signaling controls pancreatic cell differentiation. *Nature* **400**, 877-881.

Azizoglu, D. B., Braitsch, C., Marciano, D. K. and Cleaver, O. (2017). Afadin and RhoA control pancreatic endocrine mass via lumen morphogenesis. *Genes Dev.* **21**, 2376-2390.

Bankaitis, E. D., Bechard, M. E. and Wright, C. V. E. (2015). Feedback control of growth, differentiation, and morphogenesis of pancreatic endocrine progenitors in an epithelial plexus niche. *Genes Dev.* **29**, 2203-2216.

Bechard, M. E., Bankaitis, E. D., Hipkens, S. B., Ustione, A., Piston, D. W., Yang, Y.-P., Magnuson, M. A. and Wright, C. V. (2016). Precommitment low-level Neurog3 expression defines a long-lived mitotic endocrine-biased progenitor pool that drives production of endocrine-committed cells. *Genes Dev.* **30**, 1852-1865.

Cebola, I., Rodríguez-Seguí, S. A., Cho, C. H.-H., Bessa, J., Rovira, M., Luengo, M., Chhatriwala, M., Berry, A., Ponsa-Cobas, J., Maestro, A. et al. (2015). TEAD and YAP regulate the enhancer network of human embryonic pancreatic progenitors. *Nat. Cell Biol.* **17**, 615-626.

Clark, B. S., Cui, S., Miesfeld, J. B., Klezovitch, O., Vasioukhin, V. and Link, B. A. (2012). Loss of Llgl in retinal neuroepithelia reveals links between apical domain size, Notch activity and neurogenesis. *Development* **139**, 1599-1610.

Cortijo, C., Gouzi, M., Fadel, T. and Grapin-Botton, A. (2012). Planar cell polarity controls pancreatic beta cell differentiation and glucose homeostasis. *Cell Reports* **2**, 1593-1606.

Del Bene, F., Wehman, A. M., Link, B. A. and Baier, H. (2008). Regulation of Neurogenesis by interkinetic nuclear migration through an apical-basal notch gradient. *Cell* **134**, 1055-1065.

De Vas, M. G., Kopp, J. L., Heliot, C., Sander, M., Cereghini, S. and Haumaitre, C. (2015). Hnf1b controls pancreas morphogenesis and the generation of Ngn3$^+$ endocrine progenitors. *Development* **142**, 871-882.

Ebrahim, S., Fujita, T., Millis, B. A., Kozin, E., Ma, X., Kawamoto, S., Baird, M. A., Davidson, M., Yonemura, S., Hisa, Y. et al. (2013). NMII forms a contractile transcellular sarcomeric network to regulate apical cell junctions and tissue geometry. *Curr. Biol.* **23**, 731-736.

Gorfinkiel, N. and Blanchard, G. B. (2011). Dynamics of actomyosin contractile activity during epithelial morphogenesis. *Curr. Opin. Cell Biol.* **23**, 531-539.

Gouzhi, M., Kim, Y. H., Katsumoto, K., Johansson, K. and Grapin-Botton, A. (2011). Neurogenin3 initiates stepwise delamination of differentiating endocrine cells during pancreas development. *Dev. Dyn.* **240**, 589-604.

Gradwohl, G., Dierech, A., LeMeur, M. and Gillemot, F. (2000). Neurogenin3 is required for the development of the four endocrine cell lineages. *Proc. Natl. Acad. Sci. USA* **97**, 1607-1611.

Grapin-Botton, A. (2005). Ductal Cells of the pancreas. *Int. J. Biochem. Cell Biol.* **37**, 504-510.

Gu, G., Dubauskiate, J. and Melton, D. (2002). Direct evidence for the pancreatic lineage: Ngn3$^+$ cells are islet progenitors and are distinct from duct progenitors. *Development* **129**, 2447-2457.

Gurdon, J. B. (1988). A community effect in animal development. *Nature* **336**, 772-774.

Heisenberg, C.-P. and Bellaïche, Y. (2013). Forces in tissue morphogenesis and patterning. *Cell* **153**, 948-962.

Hick, A.-C., van Eyll, J. M., Sabine, C., Forez, C., Passante, L., Kohara, H., Nagasawa, T., Vanderhaeghen, P., Courtoy, P., Rousseau, G. et al. (2009). Mechanism of primitive duct formation in the pancreas and submandibular glands: a role for SDF-1. *BMC Dev. Biol.* **9**, 66.

Kesavan, G., Sand, F. W., Greiner, T. U., Johansson, J. K., Kobberup, S., Xunwei, W., Brakebusch, C. and Semb, H. (2009). Cdc42-mediated tubulogenesis controls cell specification. *Cell* **139**, 791-801.

Kim, K., Ossipova, O. and Sokol, S. Y. (2015). Neural crest specification by inhibition of the ROCK/Myosin II pathway. *Stem Cells* **33**, 674-685.

Kopp, J. L., Dubois, C. L., Schaffer, A. E., Hao, E., Shih, H. P., Seymour, P. A., Ma, J. and Sander, M. (2011). Sox9$^+$ ductal cells are multipotent progenitors throughout development but do not produce new endocrine cells in the normal or injured adult pancreas. *Development* **138**, 653-665.

Kovacs, M., Toth, J., Hetenyi, C., Malnasi-Csizmadia, A. and Sellers, J. R. (2004) Mechanism of blebbistatin inhibition of myosin II. *J. Biol. Chem.* **279**, 35557-63.

Johansson, K. A., Dursun, U., Jordan, N., Gu, G., Beermann, F., Gradwohl, G. and Grapin-Botton, A. (2007). Temporal control of neurogenin3 activity in pancreas progenitors reveals competence windows for the generation of different endocrine cell types. *Dev. Cell* **12**, 457-465.

Lee, J. C., Smith, S. B., Watada, H., Lin, J., Scheel, D., Wang, J., Mirmira, R. G. and German, M. S. (2001). Regulation of the pancreatic pro-endocrine gene neurogenin3. *Diabetes* **50**, 928-936.

Li, L. and Xie, T. (2005). Stem cell niche: structure and function. *Annu. Rev. Cell Dev. Biol.* **21**, 605-631.

Li, Z., Dong, X., Wang, Z., Liu, W., Deng, N., Ding, Y., Tang, L., Hla, T., Zeng, R., Li, L. et al. (2005). Regulation of PTEN by Rho small GTPases. *Nat. Cell Biol.* **7**, 399-404.

Löf-Öhlin, Z. M., Nyeng, P., Bechard, M. E., Hess, K., Bankaitis, E., Greiner, T. U., Ameri, J., Wright, C. V. and Semb, H. (2017). EGFR signaling controls cellular fate and pancreatic morphogenesis by regulating apicobasal polarity. *Nat. Cell Biol.* **19**, 1313-1325.

Maekawa, M., Ishizaki, T., Boku, S., Watanabe, N., Fujita, A., Iwamatsu, A., Obinata, T., Ohashi, K., Mizuno, K. and Narumiya, S. (1999). Signaling from Rho to the actin cytoskeleton through protein kinases ROCK and LIM-kinase. *Science* **285**, 895-898.

Magenheim, J., Klein, A. M., Stanger, B. Z., Ashery-Padan, R., Sosa-Pineda, B., Gu, G. and Dor, Y. (2011). Ngn3$^+$ endocrine progenitor cells control the fate and morphogenesis of pancreatic ductal epithelium. *Dev. Biol.* **359**, 26-36.

Marinari, E., Mehonic, A., Curran, S., Gale, J., Duke, T. and Baum, B. (2012). Live-cell delamination counterbalances epithelial growth to limit tissue overcrowding. *Nature* **484**, 542-545.

Martin, A. C. and Goldstein, B. (2014). Apical constriction: themes and variations on a cellular mechanism driving morphogenesis. *Development* **141**, 1987-1998.

Marty-Santos, L. and Cleaver, O. (2016). Pdx1 regulates pancreas tubulogeneis and E-cadherin expression. *Development* **143**, 101-112.

McBeath, R., Pirone, D. M., Nelson, C. M. and Chen, C. S. (2004). Cell shape, cytoskeletal tension, and RhoA regulate stem cell lineage commitment. *Dev. Cell.* **6**, 483-495.

Milano, J., McKay, J., Dagenais, C., Foster-Brown, L., Pognan, F., Gradient, R., Jacobs, R., Zacco, A., Greenberg, B. and Ciacco, P. (2004). Modulation of Notch Processing by γ-secretase inhibitors causes intestinal goblet cell metaplasia and induction of genes known to specify gut secretory lineage differentiation. *Toxicol. Sci.* **82**, 341-358.

Miyatsuka, T., Kosaka, Y., Kim, H. and German, M. S. (2011). Neurogenin3 inhibits proliferation in endocrine progenitors by inducing Cdkn1a. *Proc. Natl. Acad. Sci. USA* **108**, 185-190.
Murtaugh, L. C., Stanger, B. Z., Kwan, K. M. and Melton, D. A. (2003). Notch signaling controls multiple steps of pancreatic differentiation. *Proc. Natl. Acad. Sci. USA* **100**, 14920-14925.
Nakayama, M., Amano, M., Kaysumi, A., Kaneko, T., Kawabata, S., Takefuji, M. and Kaibuchi, K. (2005). Rho-kinase and myosin II activities are required for cell type and environment specific migration. *Genes Cells* **10**, 107-117.
Nakayama, M., Goto, T. M., Sugimoto, M., Nishimura, T., Shinagawa, T., Ohno, S., Amano, M. and Kaibuchi, K. (2008). Rho-kinase phosphorylates PAR-3 and disrupts PAR complex formation. *Dev. Cell* **14**, 205-215.
Ninov, N., Borius, M. and Stainier, D. Y. R. (2012). Different levels of Notch signaling regulate quiescence, renewal, and differentiation in pancreatic endocrine progenitors. *Development* **139**, 1557-1567.
Pan, F. C. and Wright, C. (2011). Pancreas organogenesis: from bud to plexus to gland. *Dev. Dyn.* **240**, 530-565.
Petzold, K. M., Naumann, H. and Spagnoli, F. M. (2013). Rho signaling restriction by thee RhoGAP Stard13 integrates growth and morphogenesis in the pancreas. *Development* **140**, 126-135.
Pierreux, C. E., Poll, A. V., Kemp, C. R., Clotman, F., Maestro, M. A., Cordi, S., Ferrer, J., Leyns, L., Rousseau, G. G. and Lemaigre, F. P. (2006). The transcription factor hepatocyte nuclear factor-6 controls the development of pancreatic ducts in the mouse. *Gastroenterology* **130**, 532-541.
Qu, X., Afelik, S., Jensen, J. N., Bukys, M. A., Kobberup, S., Schmerr, M., Xiao, F., Nyeng, P., Veronica Albertoni, M., Grapin-Botton, A. et al. (2013). Notch-mediated post-translational control of Ngn3 protein stability regulates pancreatic patterning and cell fate commitment. *Dev. Biol.* **376**, 1-12.
Rieck, S., Bankaitis, E. D. and Wright, C. V. E. (2012). Lineage determinants in early endocrine development. *Semin. Cell Dev. Biol.* **23**, 673-684.
Riento, K. and Ridley, A. J. (2003). Rocks: multifunctional kinases in cell behaviors. *Nat. Rev. Mol. Cell Biol.* **4**, 446-456.
Schwitzgebel, V. M., Scheel, D. W., Conners, J. R., Kalamaras, J., Lee, J. E., Anderson, D. J., Sussel, L., Johnson, J. D. and German, M. S. (2000). Expression of neurogenin3 reveals an islet cell precursor population in the pancreas. *Development* **127**, 3533-3542.
Serup, P. (2012). Signaling pathways regulating murine pancreas development. *Semin. Cell Dev. Biol.* **23**, 663-672.
Shih, H. P. and Sander, M. (2014). Pancreas development ex vivo: culturing embryonic pancreas explants on permeble culture inserts, with fibronectin-coated glass microwells, or embedd in thre-dimensional matrigel™. *Methods Mol. Biol.* **1210**, 229-237.
Shih, H. P., Kopp, J. L., Sandhu, M., Dubois, C. L., Seymour, P., Grapin-Botton, A. and Sander, M. (2012). A Notch-dependent molecular circuitry initiates pancreatic endocrine and ductal cell differentiation. *Development* **139**, 2488-2499.
Sordella, R., Jiang, W., Chen, G. C., Curto, M. and Settleman, J. (2003). Modulation of Rho GTPase signaling regulates a switch between adipogenesis and myogenesis. *Cell* **113**, 147-158.
Straight, A. F., Cheung, A., Limouze, J., Chen, I., Westwood, N. J., Sellers, J. R. and Mitchison, T. J. (2003). Dissecting temporal and spatial control of cytokinesis with a myosin II inhibitor. *Science* **299**, 1743-1747.
Uehata, M., Ishizaki, T., Satoh, H., Ono, T., Kawahara, T., Morishita, T., Tamakawa, H., Yamagami, K., Inui, J., Maekawa, M. et al. (1997). Calcium sensitization of smooth muscle mediated by a Rho-associated kinase in hypertension. *Nature* **389**, 990-994.
Villasenor, A., Chong, D. C., Henkemeyer, M. and Cleaver, O. (2010). Epithelial dynamics of pancreatic branching morphogenesis. *Development* **137**, 4295-4305.
Wang, J., Kilic, G., Aydin, M., Burke, Z., Oliver, G. and Sosa-Pineda, B. (2005). Prox1 activity controls pancreas morphogenesis and participates in the production of “secondary transition” pancreatic endocrine cells. *Dev. Biol.* **286**, 182-194.
Wang, S., Hecksher-Sorensen, J., Xu, Y., Zhao, A., Dor, Y., Rosenberg, L., Serup, P. and Gu, G. (2008). Myt1 and Ngn3 form a feed-forward expression loop to promote endocrine islet cell differentiation. *Dev. Biol.* **317**, 531-540.
Wang, Y., Zheng, X. R., Riddick, N., Bryden, M., Baur, W., Zhang, X. and Surks, H. K. (2009). ROCK isoform regulation of myosin phosphatase and contractility in vascular smooth muscle cells. *Circ. Res.* **104**, 531-540.
Wang, S., Yan, J., Anderson, D., Xu, Y., Kanal, M. C., Cao, Z., Wright, C. and Gu, G. (2010). Neurog3 gene dosage regulates allocation of endocrine and exocrine cell fates in the developing mouse pancreas. *Dev. Biol.* **339**, 26-37.
Watanabe, N., Kato, T., Fujita, A., Ishizaki, T. and Narumiya, S. (1999). Cooperation between mDia1 and ROCK in Rho-induced actin reorganization. *Nat. Cell Biol.* **1**, 136-143.
Westmoreland, J. J., Kilic, G., Sartain, C., Sirma, S., Blain, J., Rehg, J., Harvey, N. and Sosa-Pineda, B. (2012). Pancreas-specific deletion of Prox1 affects development and disrupts homeostasis of the exocrine pancreas. *Gastroenterology* **142**, 999-1009.
Worthylake, R. A., Lemoine, S., Watson, J. M. and Burridge, K. (2001). RhoA is required for monocyte tail retraction during transendothelial migration. *J. Cell Biol.* **154**, 147-160.

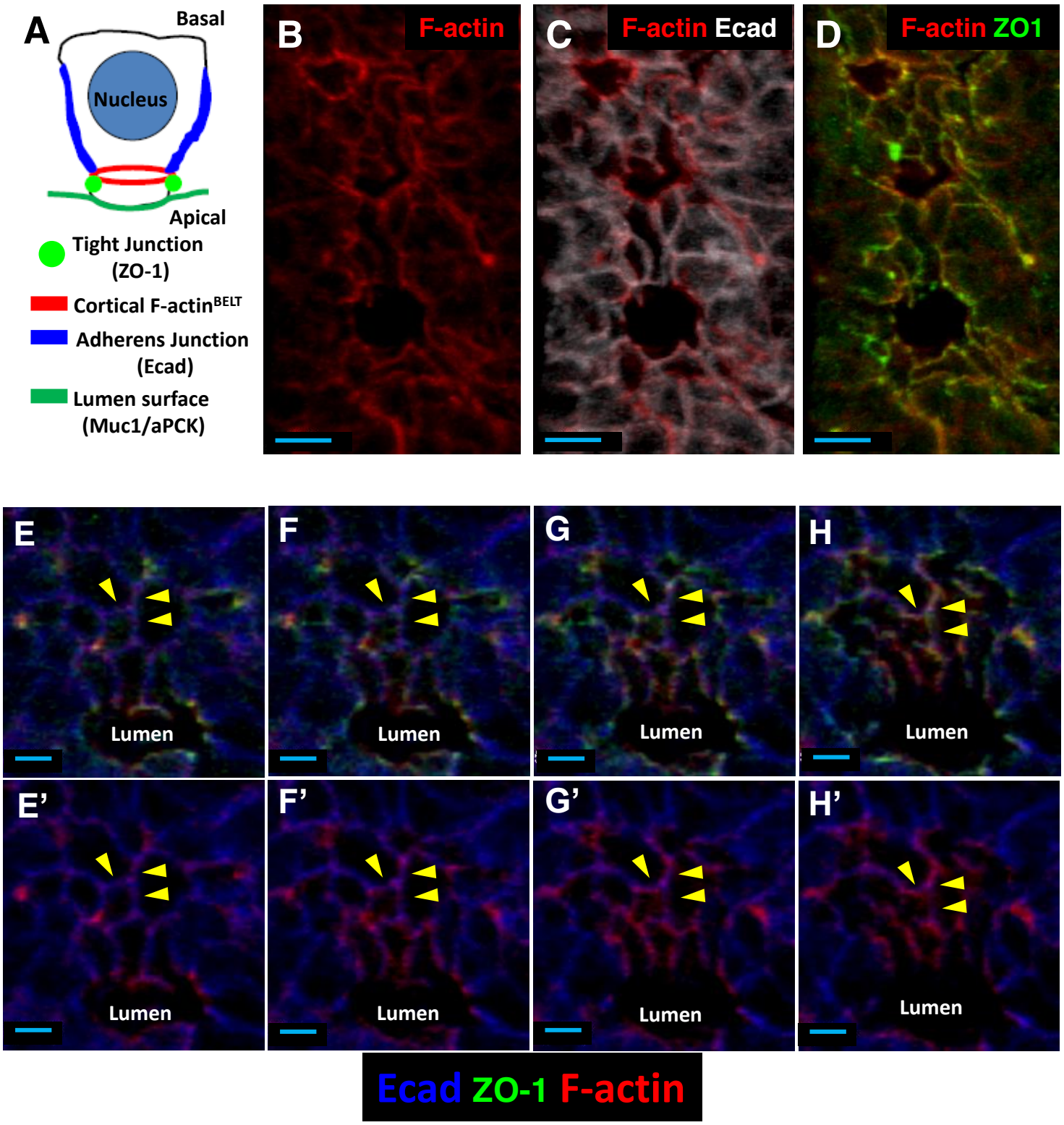

Fig. S1. Adherens and tight-junction markers demarcate a multicellular F-actin^{BELT} meshwork. (A) Schematic showing the localization of the cortical F-actin^{BELT} with respect to apical-surface (Muc1), tight junction (ZO1), and adherens-junction (Ecad). (B-D) Representative *en face* images of Ecad and ZO1 in relation to the F-actin^{BELT} network. (E-H') Confocal steps (z-direction, 1.0 μm/step) through a plane of representative epithelial cells. Note the progression from Ecad (blue) through to intense F-actin signal and ZO1. Scale Bars in *B*, *C*, & *D* are 10 μm, and 5 μm in *E-H'*.

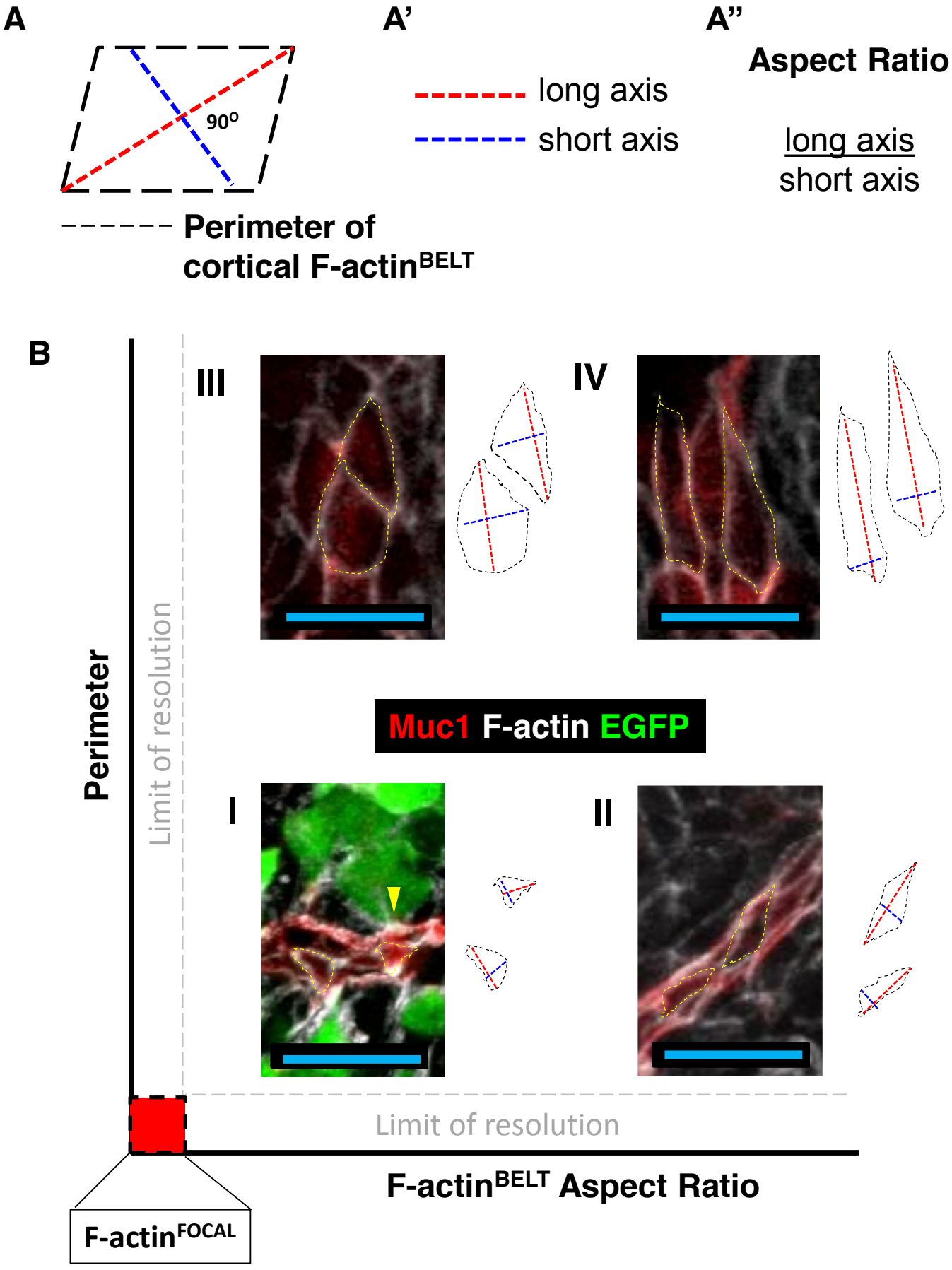

Fig. S2. F-actin^{BELT} aspect ratio versus perimeter defines the spectrum of F-actin^{BELT} sizes in epithelial populations. (A) Schematic of a typical cortical F-actin^{BELT} near apical surface an epithelial cell. Perimeter (black line) demarcates the F-actin^{BELT}. (A') Long axis (red dashed line) and short axis (blue dashed line set perpendicular (90^{O}) to the pre-set long axis) defines axial dimensions of the F-actin^{BELT}. (A'') Aspect ratio is defined by the divisional product of the long and short axis. (B) Schematic with examples of typical extremes in observed F-actin^{BELT} dimensions (F-actin^{BELT} traced in yellow dashed line). Roman numeral **I** indicates narrowed apical cortex. Roman numeral **II** indicates elongated F-actin^{BELT}. Roman numeral **III** indicates expanded F-actin^{BELT}. Roman numeral **IV** indicates expanded and elongated F-actin^{BELT}. Grey dashed line demarcates limit of resolution in x and y for accurate measurement by our methods (~2.0 μm). F-actin^{FOCAL} perimeter and aspect ratio are below minimum resolution or at the origin (red box). Yellow arrowhead marks typical F-actin^{FOCAL} structure at the apical surface of an egressing Neurog3$^{EGFP/+}$ reporting^{+} cell. Scale bars are 20 μm.

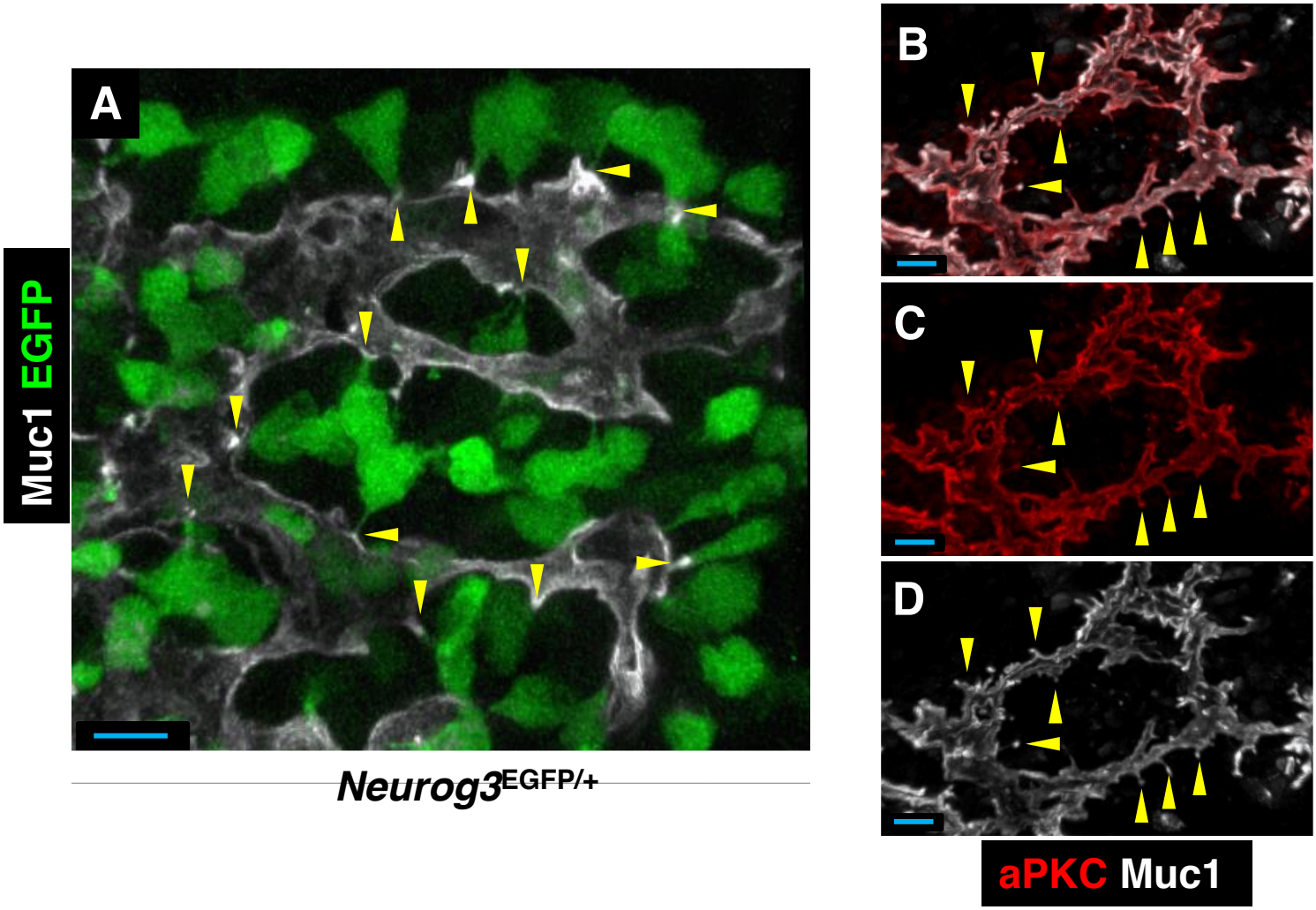

Fig. S3. Epithelially egressing endocrine cells maintain a narrow apical lumen-surface contact. (A) Representative 40x confocal z-stack of E14.5 Ngn3$^{EGFP/+}$ plexus showing apical lumen-surface contact of delaminating EGFP-reporting cells. (B-D) Immunodetection of aPCK and Muc1 showing their localization at representative Muc1^{+} F-actin^{FOCAL} structures (yellow arrowheads). Scale bars are 10 μm in *A-D*.

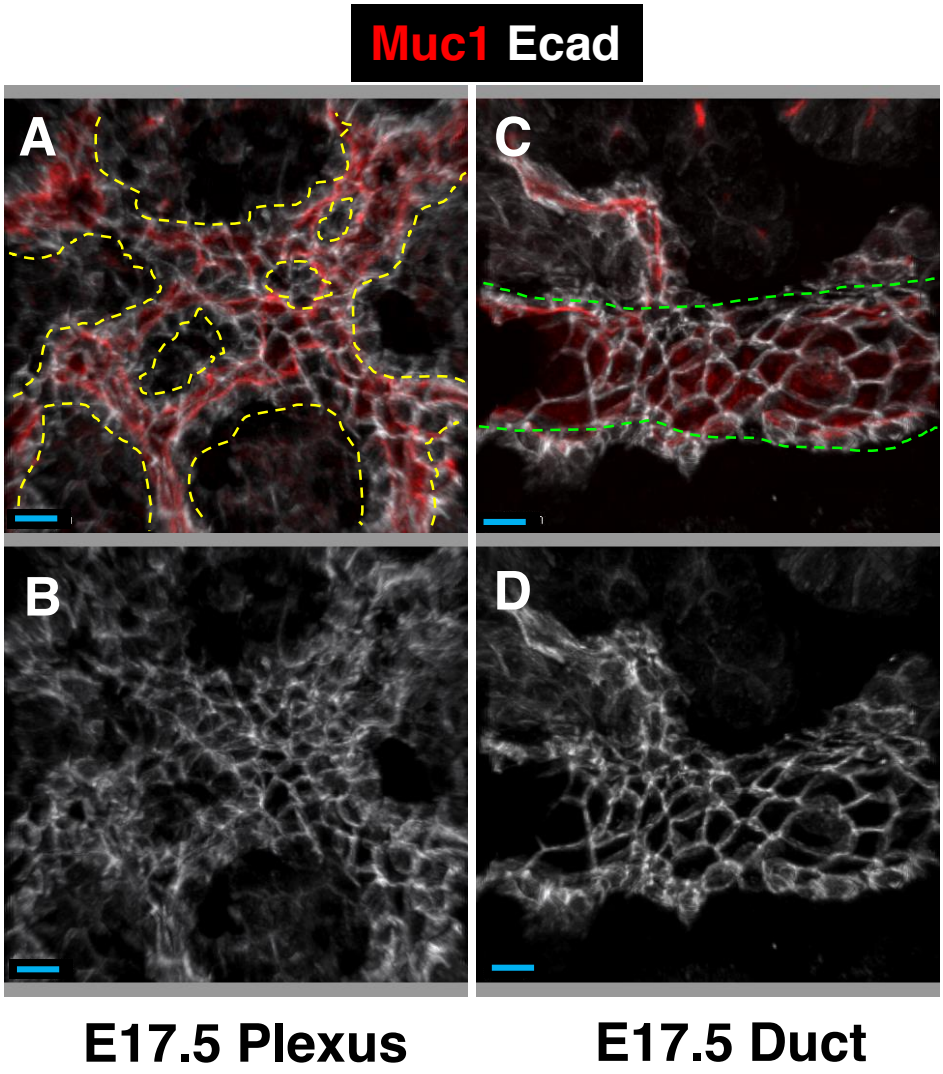

Fig. S4. E-cadherin immunolabeling shows enlargements in cell shape in the duct-state compared to the plexus. (A,B) Confocal z-stack of Muc1 and Ecad markers showing cell morphologies in the plexus at E17.5 (plexus traced by yellow dashed line). (C,D) Confocal z-stack of cell dimensions and shapes in the duct at E17.5 (duct traced by green dashed line). Scale bars are 10 μm.

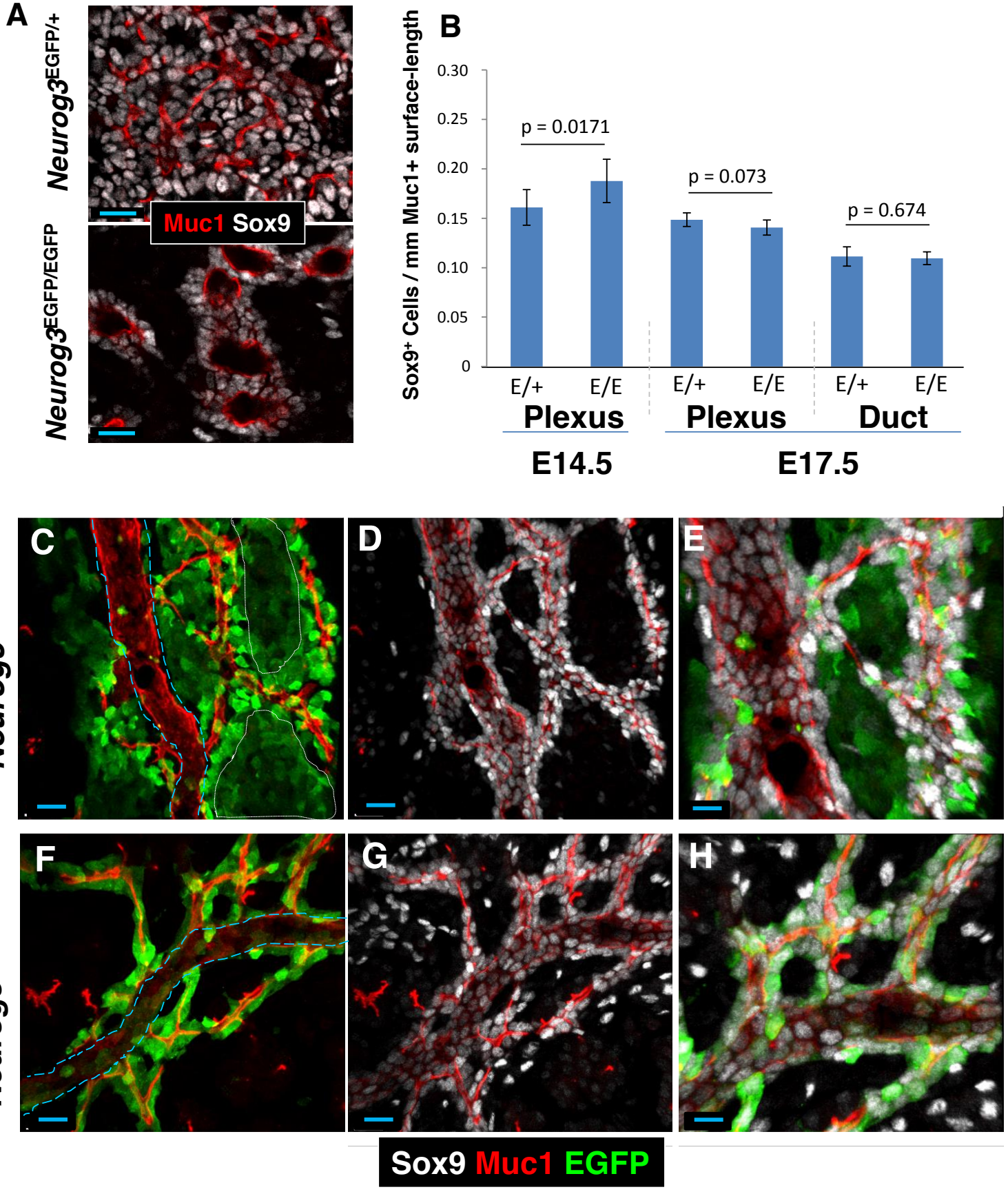

Fig. S5. Increased Sox9^{+} cell packing in the *Neurog3*-null epithelium is corrected by late gestation. (A,B) Measurements on the number of Sox9^{+} nuclei along the length of Muc1^{+} lumen *Neurog3*$^{EGFP/+}$ versus *Neurog3*$^{EGFP/EGFP}$ epithelium at E14.5 and E17.5, respectively. (C-H) Representative thick sections of Muc1, Sox9 and EGFP in duct and plexus states at E17.5. Cyan dashed lines in C and F demarcate the duct from the plexus-state, and white trace marks low EGFP expression in the forming endocrine islets. Scale bars are 20 μm in C,*D,F,G*; 10 μm in *E,H*.

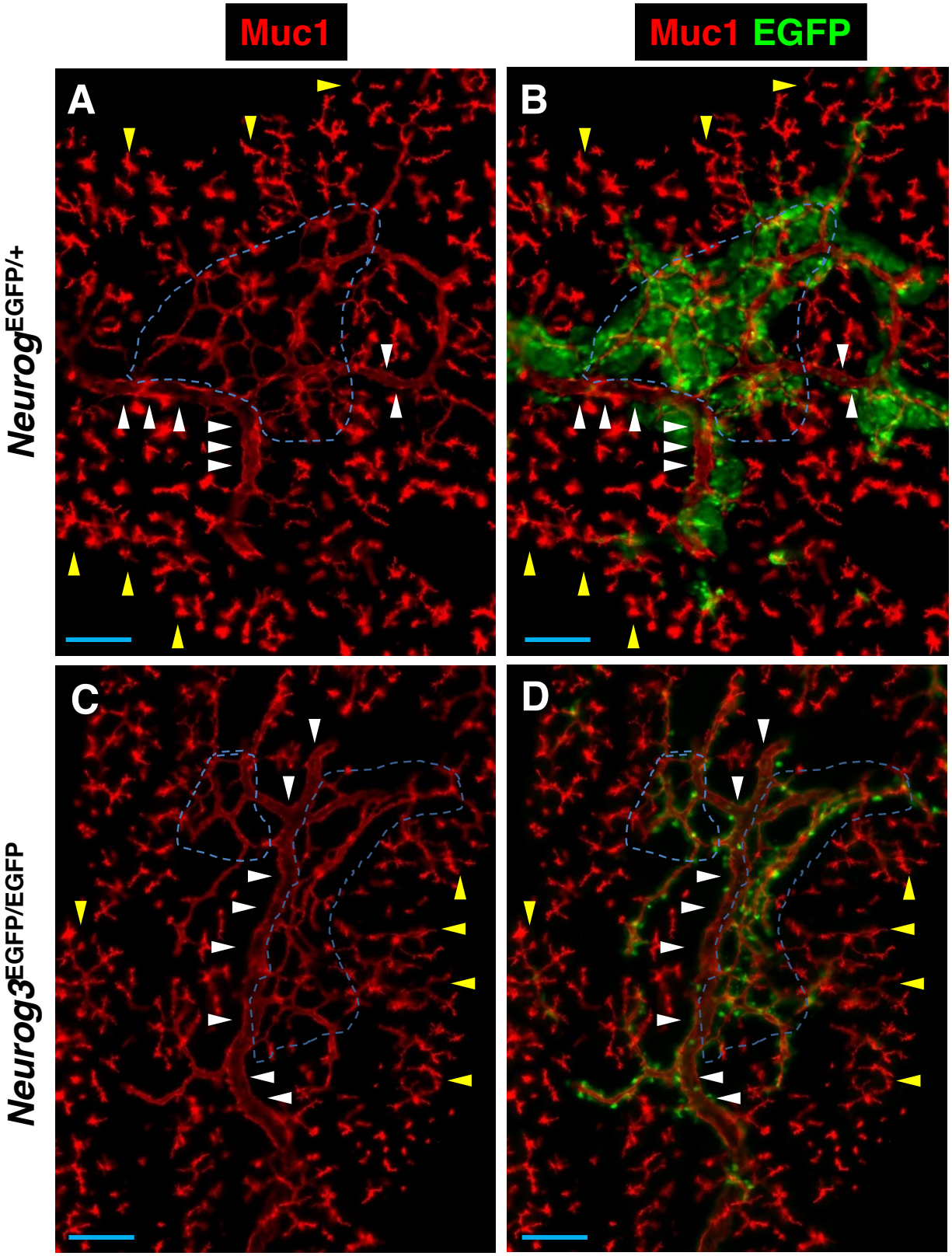

Fig. S6. *Neurog3* is broadly upregulated in cells within the plexus at late gestation. (A-D) Wide-field 10x epifluorescence images of thick-sectioned pancreas (30 μm) showing *Neurog3*-expressing cells in the plexus (blue dashed line), duct (white arrowheads), and peripheral ductal branches (yellow arrowheads) in *Neurog3*$^{EGFP/+}$ and *Neurog3*$^{EGFP/EGFP}$ epithelium at E18.5. Scale bars are 100 μm.

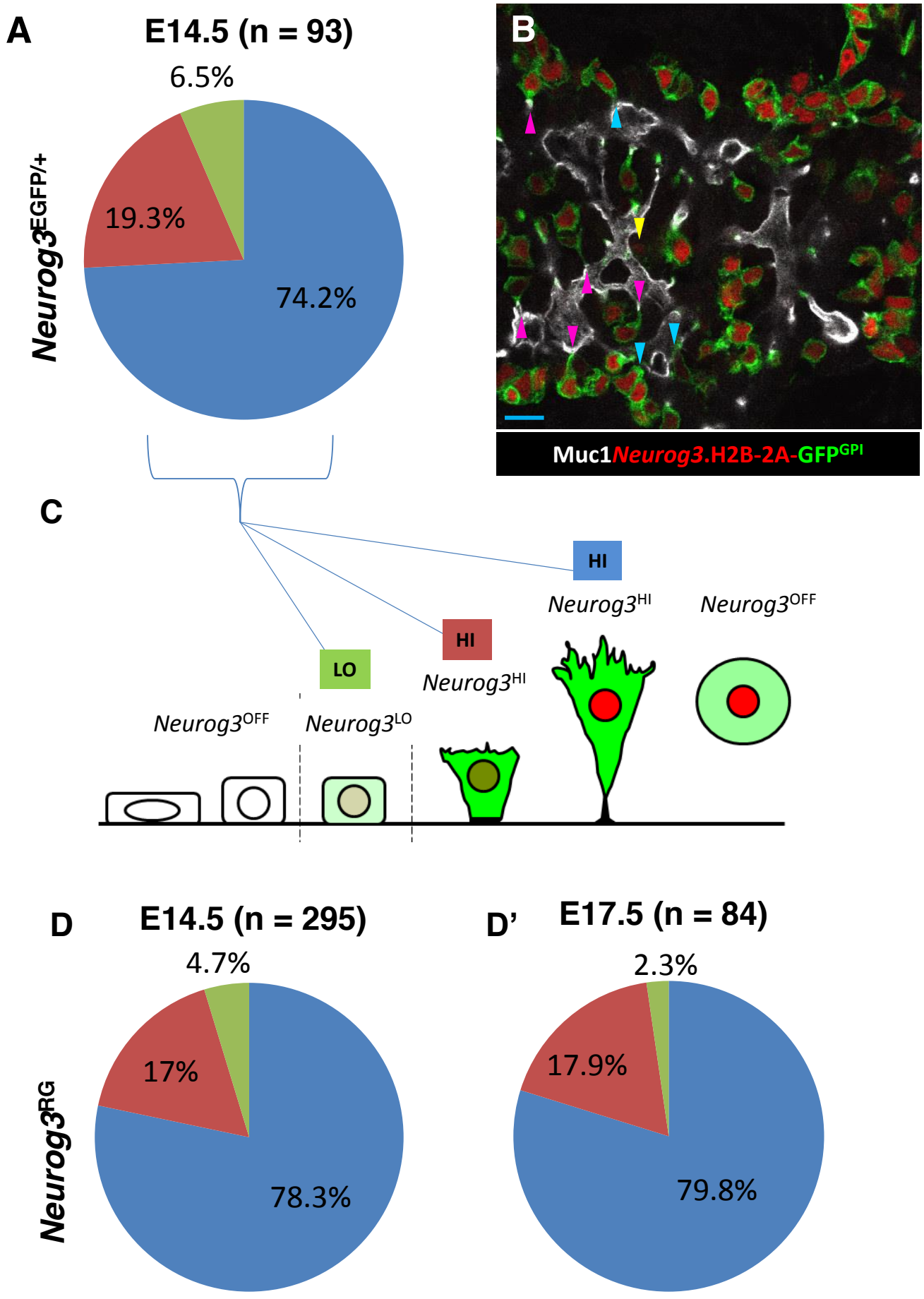

Fig. S7. Quantification of *Neurog3*-expressing states using *Neurog3* knock-in and BAC-transgenic reporter alleles. (A) Quantification of the proportions of non-apically narrowed (green), apically narrowed (red), and focalized and basally displaced (blue) *Neurog3*$^{EGFP/+}$ cells at E14.5. (B) *Neurog3*$^{RG+}$ cells in a representative z-stack labeled with Muc1 at E14.5. Yellow arrowhead marks non-apically narrowed *Neurog3*$^{RG-LO}$ cell, cyan arrowheads mark apically narrowed *Neurog3*$^{RG-HI}$ cells, pink arrowheads mark *Neurog3*$^{RG-HI}$ cells associated with F-actin^{FOCAL} structures. Scale bar is 20 μm. (C,C') Diagram of the principal cell-morphological states associated with *Neurog3*^{OFF}, *Neurog3*^{LO}, and *Neurog3*^{HI} populations, color coded to match *A*-*B*. (D,D') Percentage of non-apically narrowed (green), apically narrowed (red), and focalized and basally displaced (blue) *Neurog3*$^{RG+}$ cells at E14.5 and E17.5.

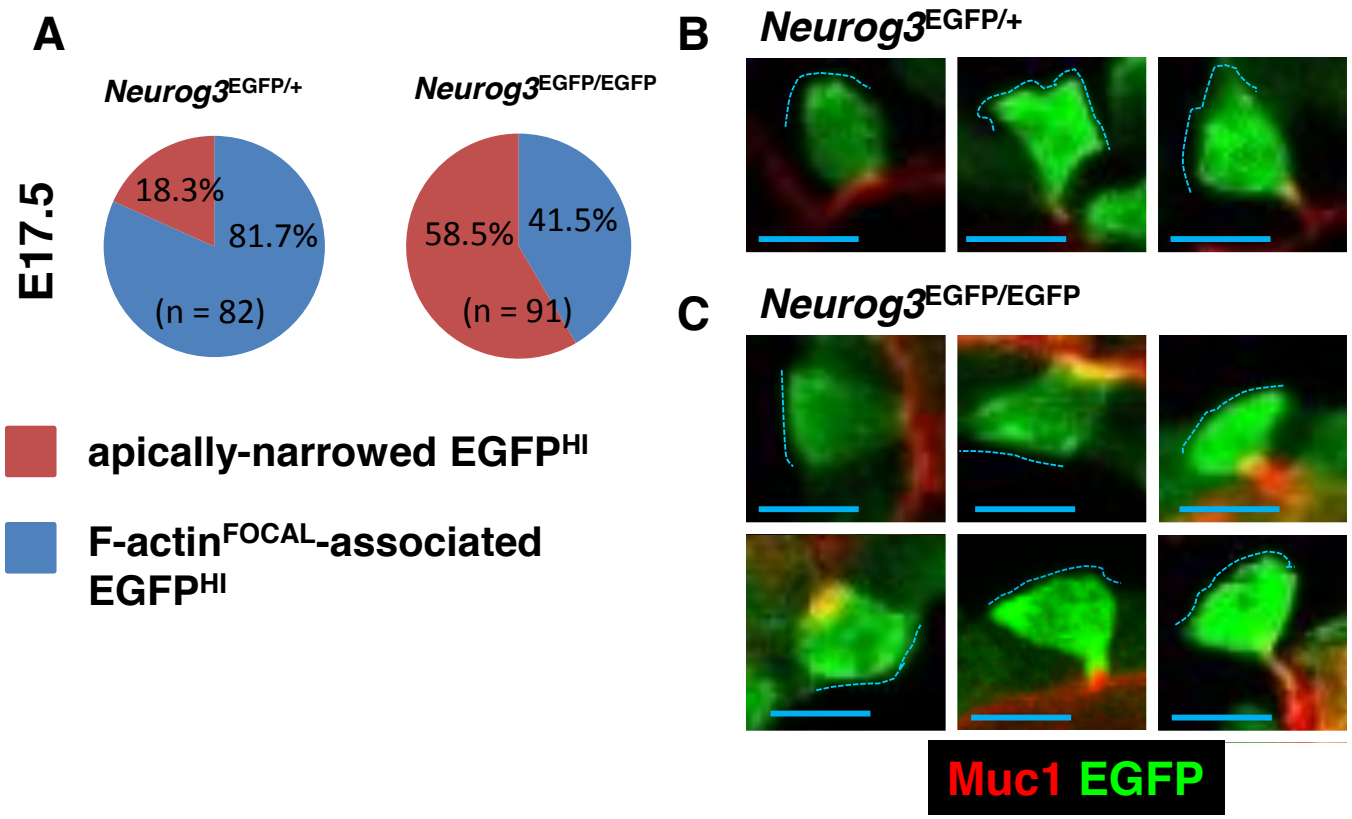

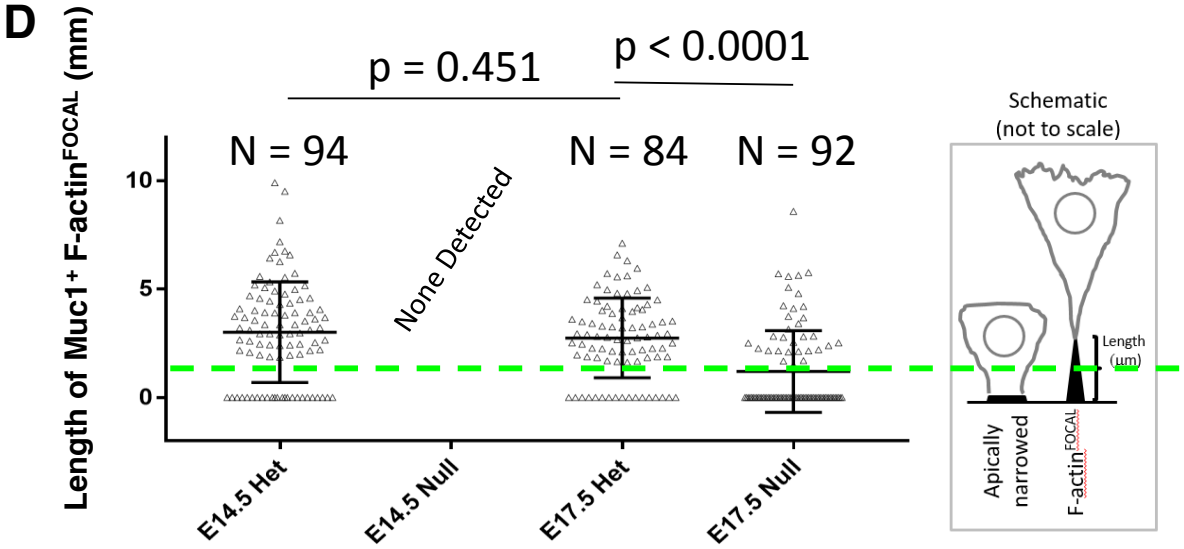

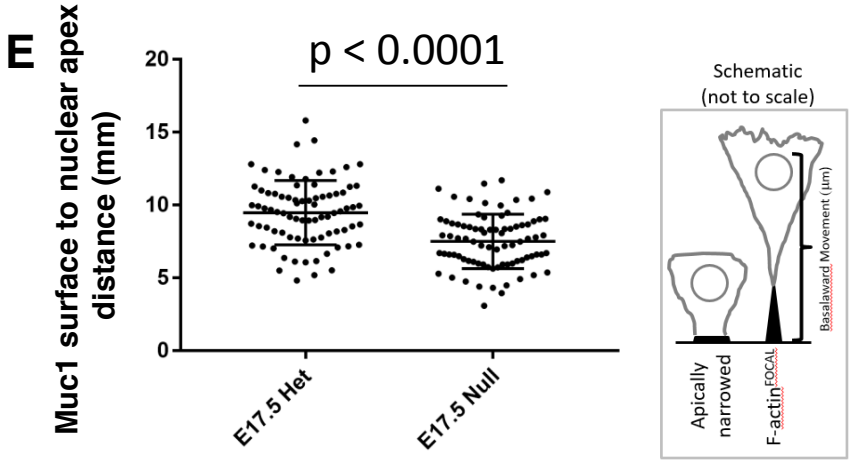

Fig. S8. *Neurog3*-deficient *Neurog3*^{HI} cells show defective apical narrowing, F-actin^{FOCAL} formation, and basalward cell movement. (A) Proportion of EGFP^{HI} cells that exhibit a narrowed apical surface versus a fully formed F-actin^{FOCAL} structure in *Neurog3*$^{EGFP/+}$ and *Neurog3*$^{EGFP/+}$ plexus at E17.5. (B) Images of EGFP^{HI} cells in *Neurog3*$^{EGFP/+}$ pancreata undergoing *Neurog3* upregulation during apical narrowing and F-actin^{FOCAL} formation. Note the migratory protrusions at the basal cell surface (dashed cyan lines). (C) Images of EGFP^{HI} cells in *Neurog3*$^{EGFP/EGFP}$ pancreata undergoing *Neurog3* upregulation during apical narrowing and F-actin^{FOCAL}-formation. (D) Measurements of the lengths of typical F-actin^{FOCAL} structures associated with EGFP^{HI} cells in *Neurog3*$^{EGFP/+}$ and *Neurog3*$^{EGFP/EGFP}$ epithelium at E14.5 and E17.5. Green dashed line indicates the distinction between an apically-narrowed surface (below line; beyond limit of accurate measure) versus a fully formed F-actin^{FOCAL} structure (above line). (E) Measurement of basalward movement was determined as the distance from the Muc1^{+} lumen surface to the basal-most aspect of the nucleus of EGFP^{HI} cells in *Neurog3*$^{EGFP/+}$ and *Neurog3*$^{EGFP/EGFP}$ epithelium at E17.5. Scale bars are 7 μm in *B,C*.

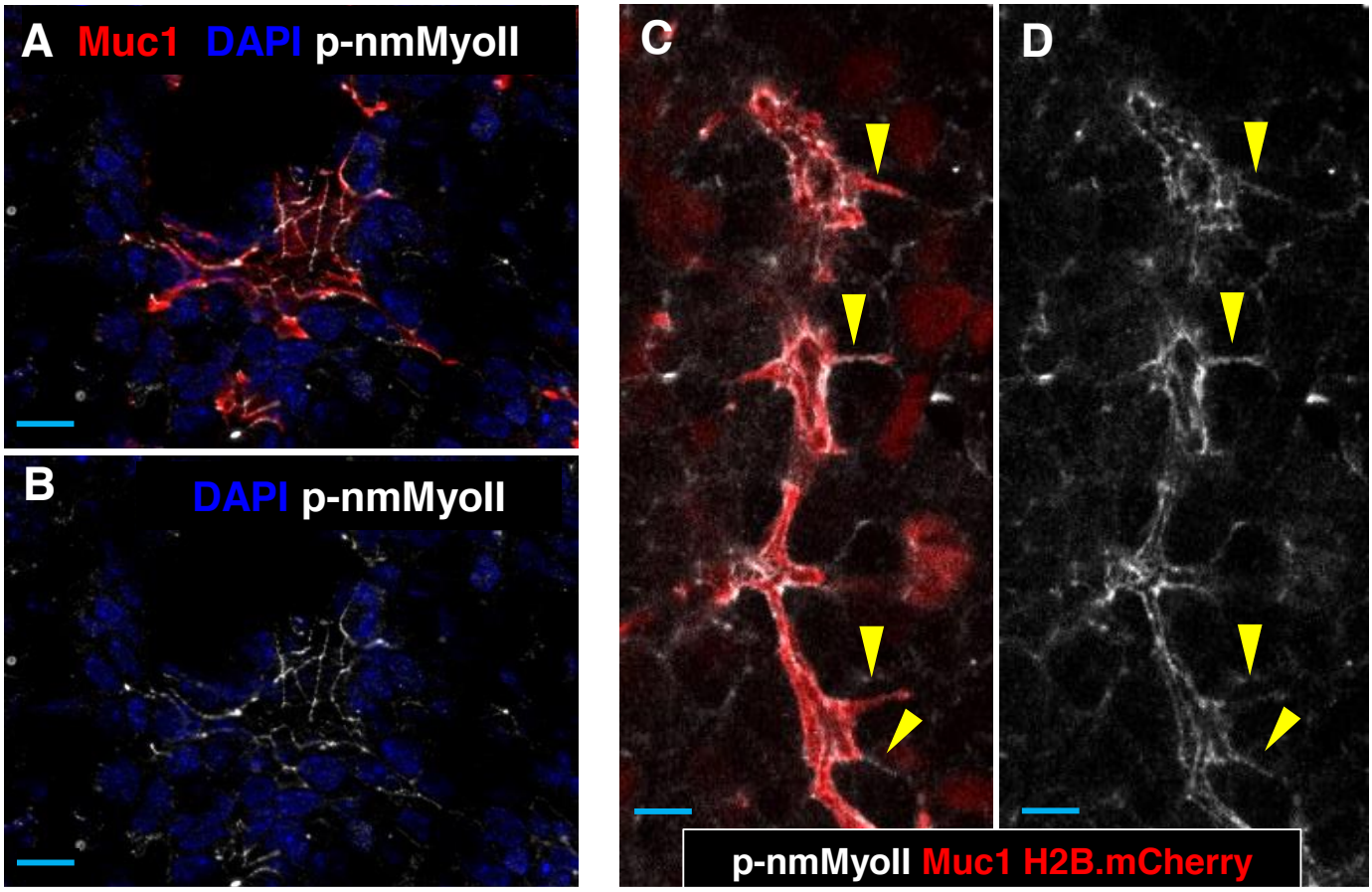

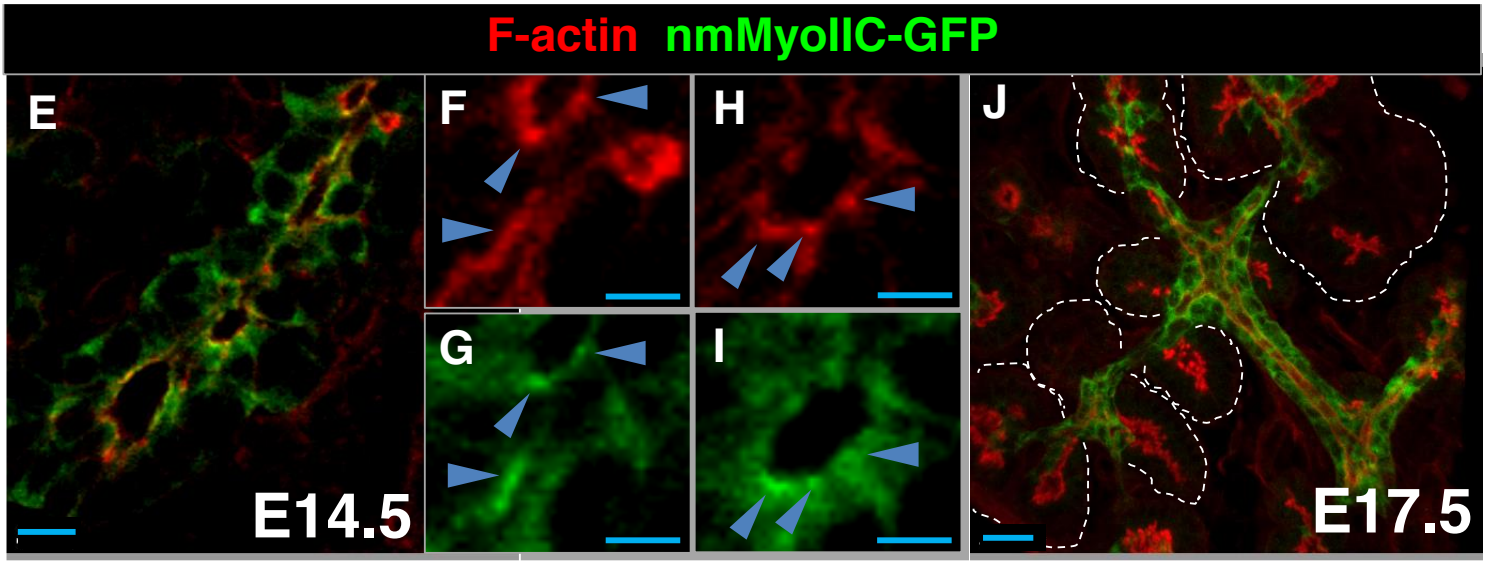

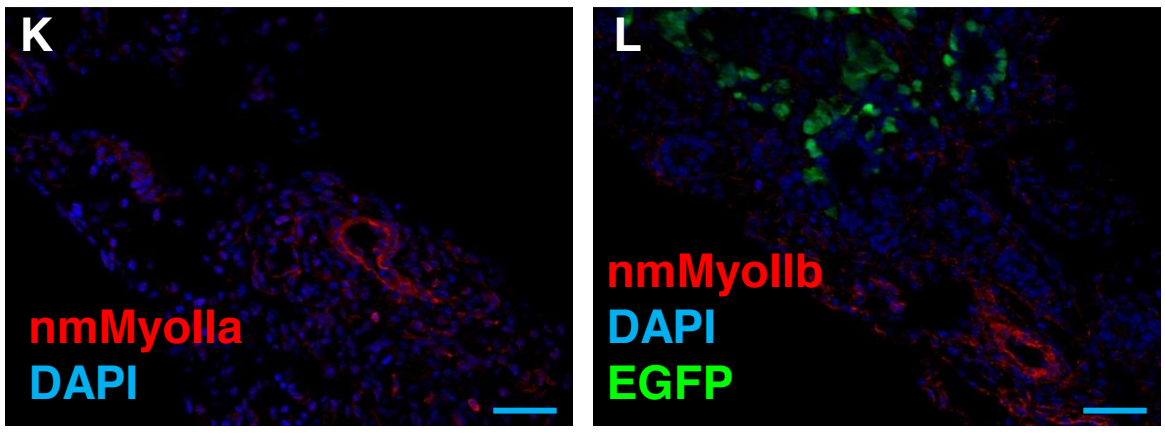

Fig. S9. nmMyoII isoforms are expressed and activated in the embryonic pancreas. (A,B) Separated fluorescence channels of p-nmMyoII along the Muc1^{+} lumen surface at E14.5. (C,D) P-nmMyoII localization along F-actin^{FOCAL} structures (yellow arrowheads) in the *Neurog3*^{RG} mouse strain. Muc1 and nuclear H2B-mCherry are shown in red, to indicate the lumen surface of *Neurog3*-expressing cells. (E) Localization of nmMyoIIC-GFP fusion protein in epithelial cells at E14.5. (F-I) Elevated nmMyoIIC-GFP signal is associated with intense phalloidin signal near the apical surface. (J) NmMyoIIC-GFP signal becomes enriched in the non-acinar epithelium by E17.5 (white dashed line demarcates acinar clusters). (K,L) nmMyoIIa and nmMyoIIb isofoms detected in the parenchyma (main blood vessels and mesenchyme) of the embryonic pancreas. EGFP signal is from the *Neurog3*$^{EGFP/+}$ knock-in mouse strain. Scale bars are 10 μm in *A*,*B*,*E*, 5 μm in *C*,*D*,*F-I*, 20 μm in *J*, and 100 μm in *K*,*L*.

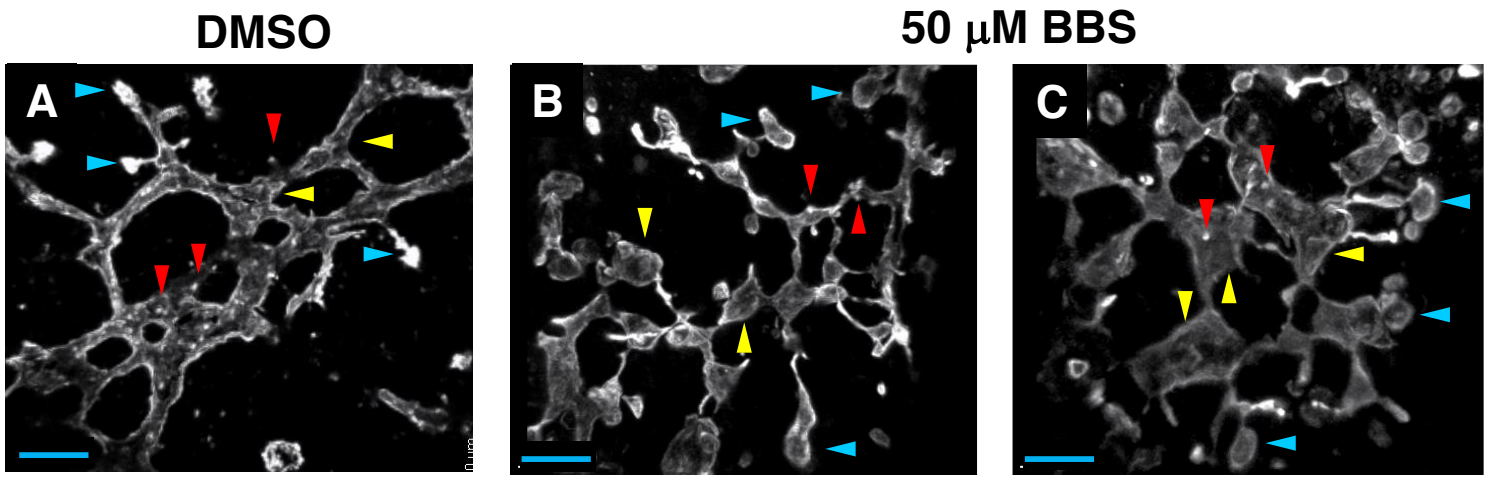

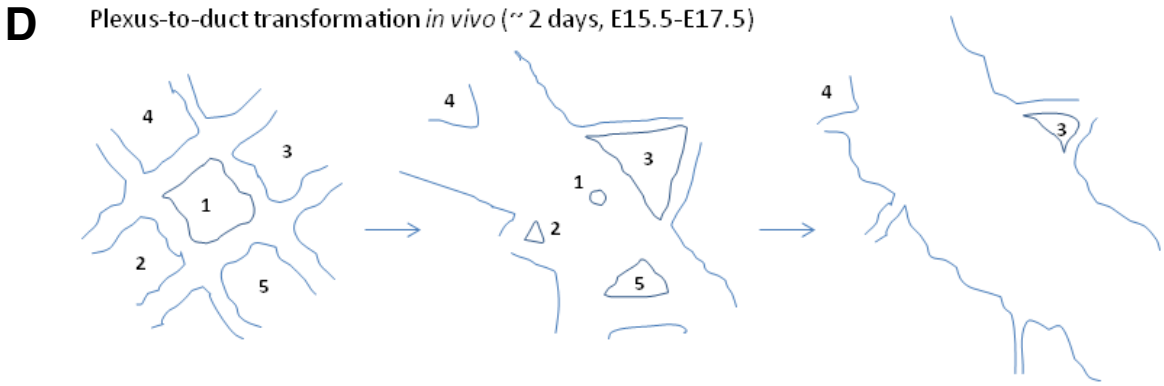

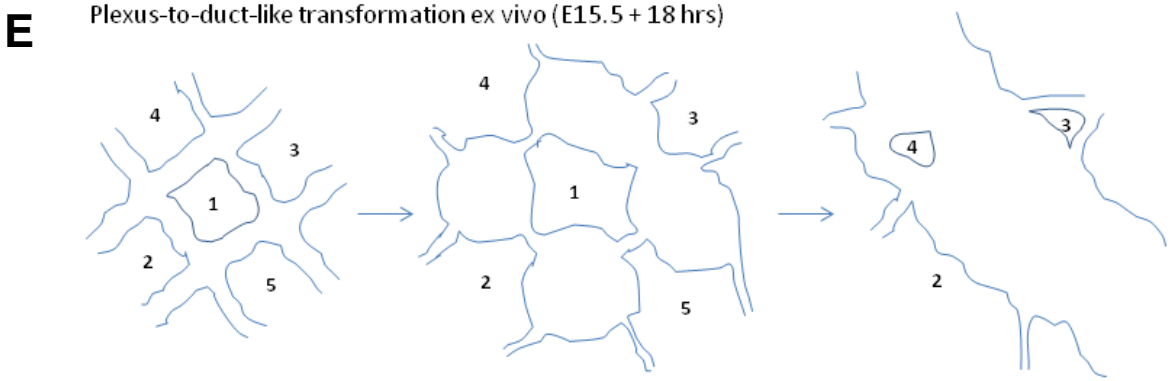

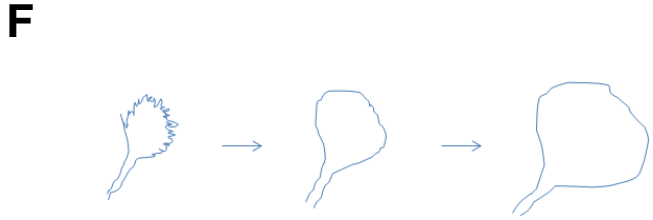

Fig. S10. NmMyoII-inhibition causes an abnormal plexus to duct-like transformation. (A) Qualities of the normal plexus state in vehicle-treated explants. (B-C) Representative images of abnormal plexus observed in BBS-treated explants. Qualities of the abnormal plexus state include localized bulb-like dilations of the epithelium (yellow arrowheads), malformed terminal acinar lumens (cyan arrowheads), and diminished numbers of F-actin^{FOCAL} structures (red arrowheads). Scale bars are 20μm. (D) Proposed diagram depicting typical plexus-to-duct transformations observed under normal (*in vivo*) and (E) nmMyoII-inhibited conditions. Note the difference in time scales. (F) Depiction of the process of acinar lumen dilation observed under nmMyoII-inhibited conditions.

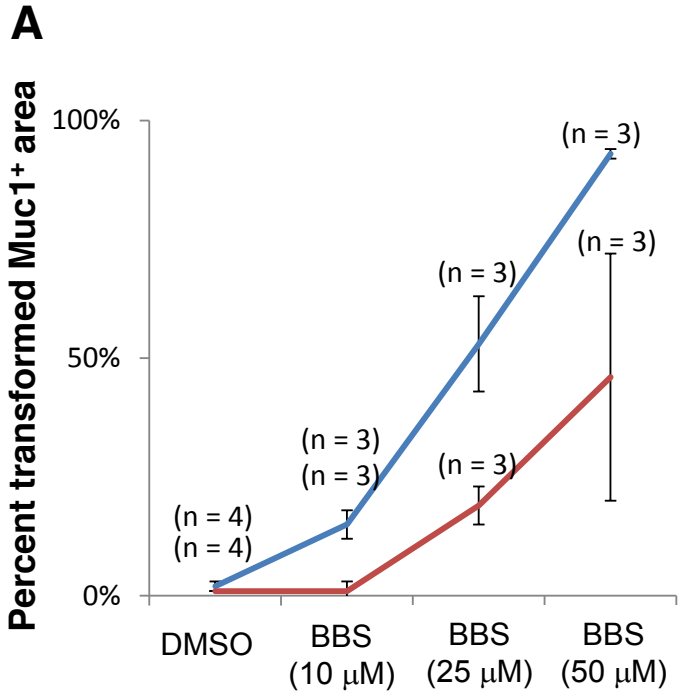

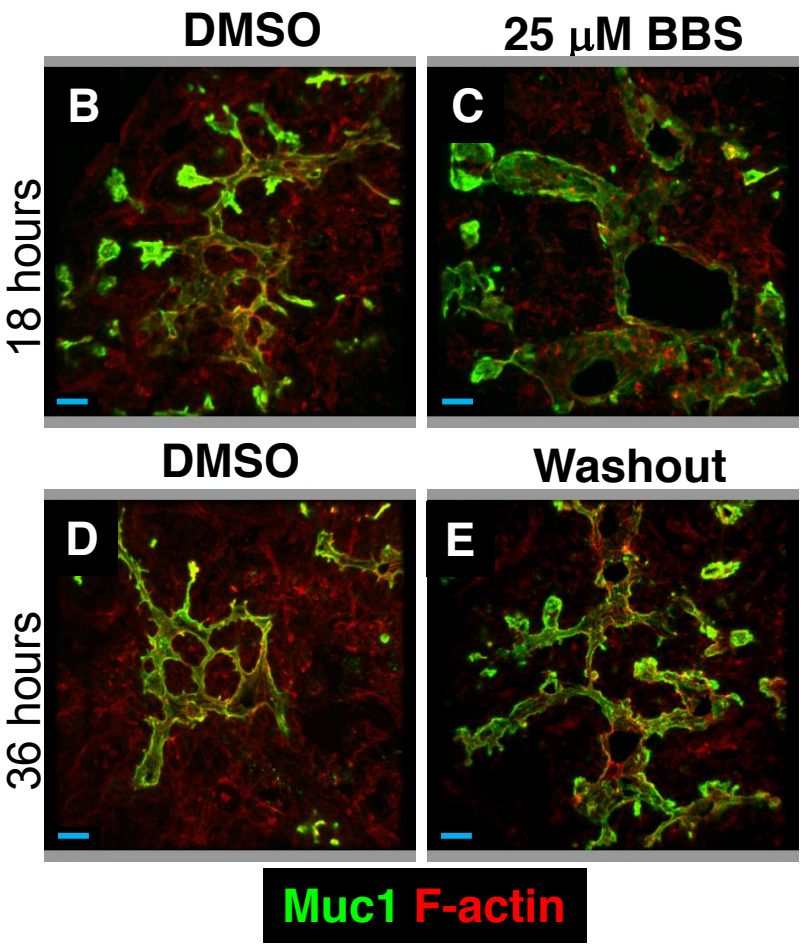

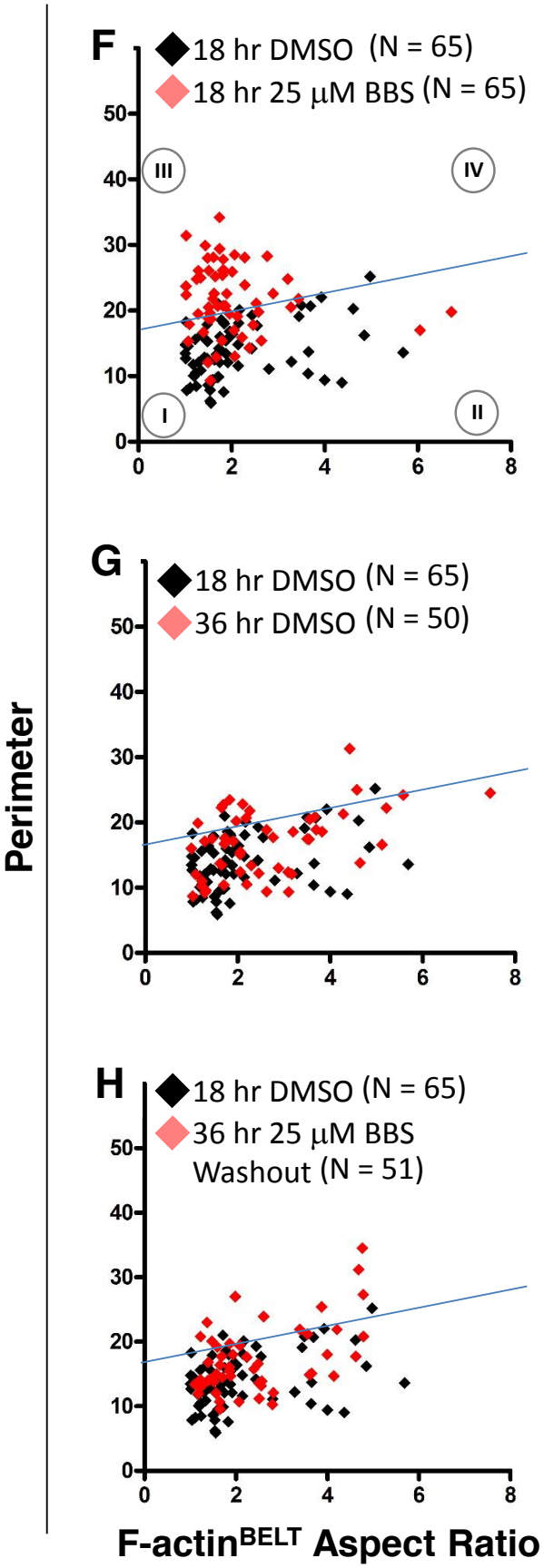

Fig. S11. Effects of BBS treatment on the plexus are dose-dependent and reversible. (A) Measurements of the relative Muc1^{+} pixel area exhibiting full duct-like transformation (red line), or abnormal plexus-state morphology (blue line), in explants grown in increasing concentrations of BBS for 18 hrs . Muc1 and F-actin localization in explants grown for 18 hr in DMSO (B), 18 hrs in 25 μM BBS (C), 36 hrs in DMSO (D), or 18 hrs in 25 μM BBS with a subsequent washout and 18 hr culture in DMSO (D). (F) Dimensions of F-actin^{BELT} in plexus treated with DMSO for 18 hrs (black dots *F*,*G*,*H*) or 25 μM BBS for 18 hrs (red dots) used as reference for *G*,*H*. (G) Dimensions of F-actin^{BELT} in plexus treated with DMSO for 36 hrs (red dots). (H) Dimensions of F-actin^{BELT} in plexus treated with 25 μM BBS for 18 hrs, with a subsequent washout and 18 hr culture in DMSO (red dots). Blue line indicates the maximum on the y-axis for F-actin^{BELT} dimensions measured in the plexus *in vivo*. Scale bars are 20 μm.

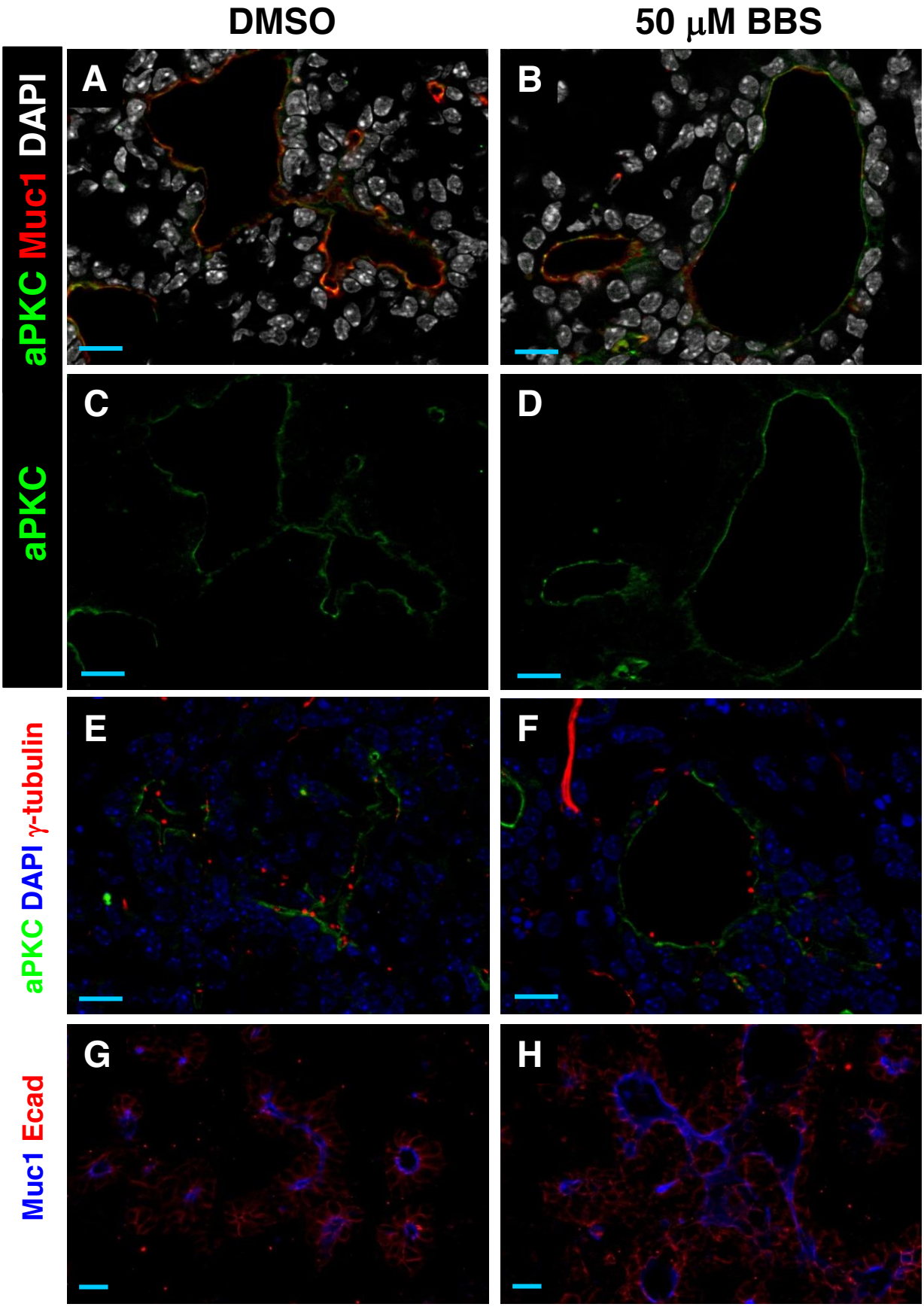

Fig. S12. Apical polarity and cell contact is maintained under nmMyoII-inhibited conditions. (A-D) Representative images of E14.5 plexus explants treated for 18 hr with DMSO or 50 μM BBS and labeled with the apical markers Muc1, and aPKC. (E,F) Untreated and treated samples labeled with the ciliary basal-body marker gamma-tubulin, which is normally localized near the $aPKC^{+}$ apical surface of epithelial cells. (G,H) E-cadherin localization in epithelial cells from treated and untreated explants. Scale bars are 10 μm.

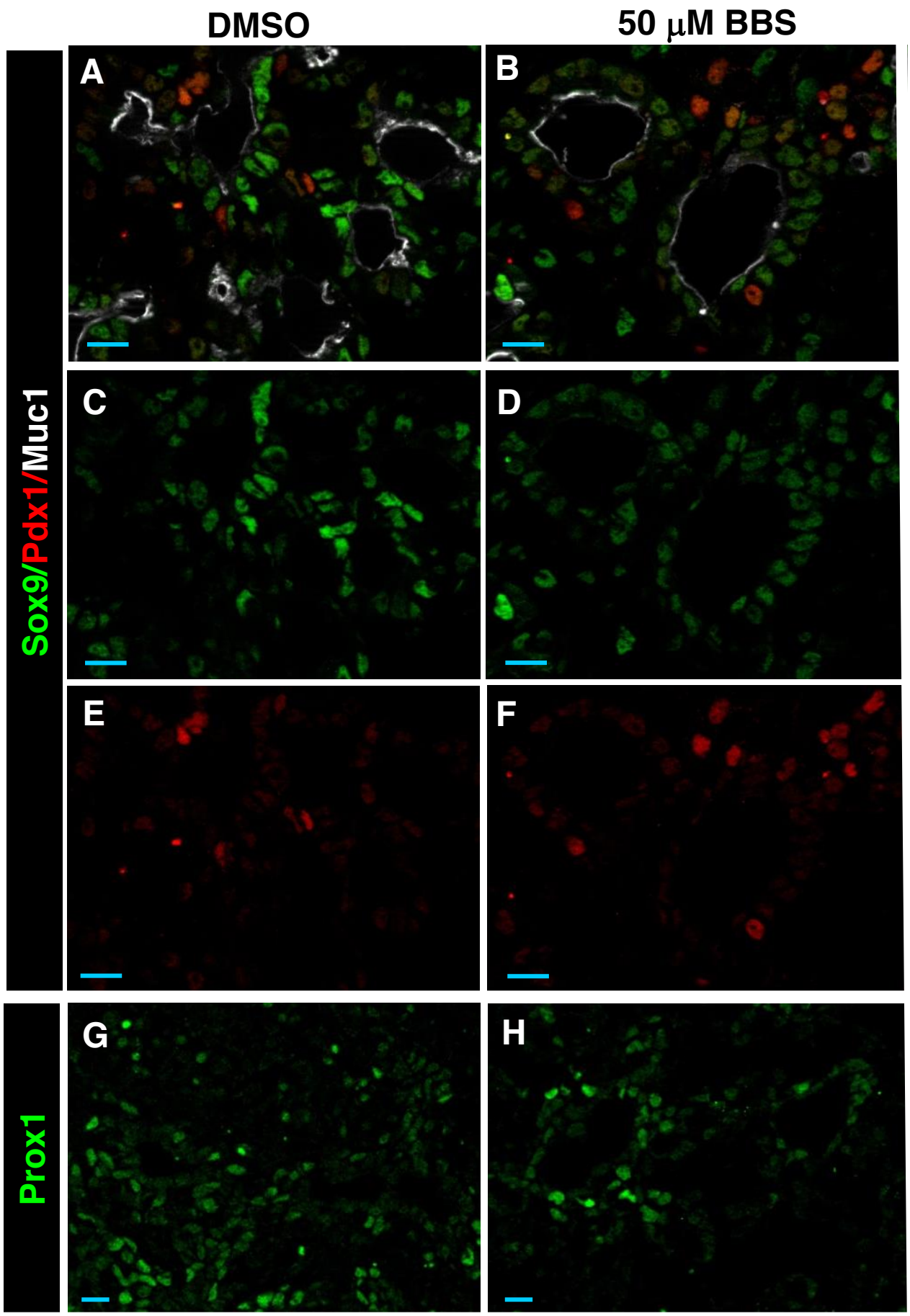

Fig. S13. Selective alterations in epithelial transcription-factor levels under nmMyoII-inhibited conditions. (A-F) Immunodetection of Sox9 and Pdx1 in plexus explants treated with DMSO or 50 μM BBS for 18 hrs. (G,H) Expression of Prox1 in plexus explants treated with DMSO or 50 μM BBS for 18 hrs. Scale bars are 10 μm.

E15.5 plexus explant, DMSO-treated

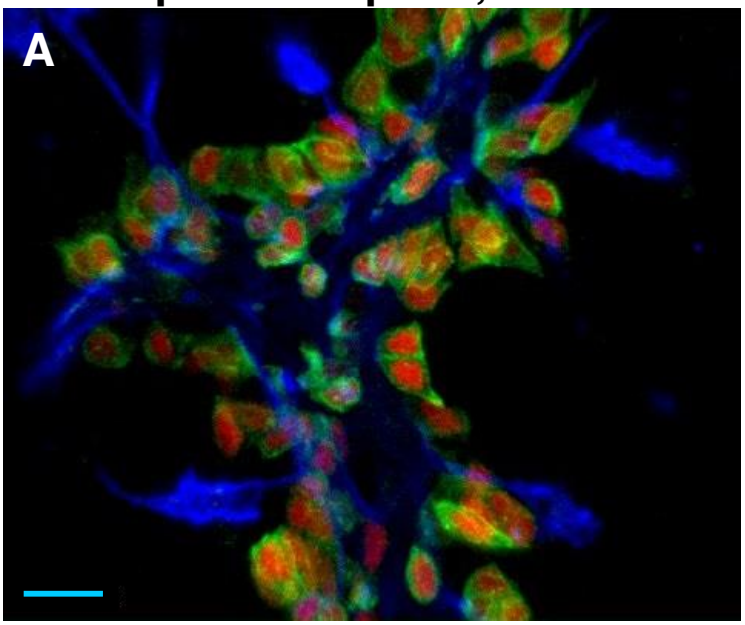

E15.5 explant, 25 μM BBS

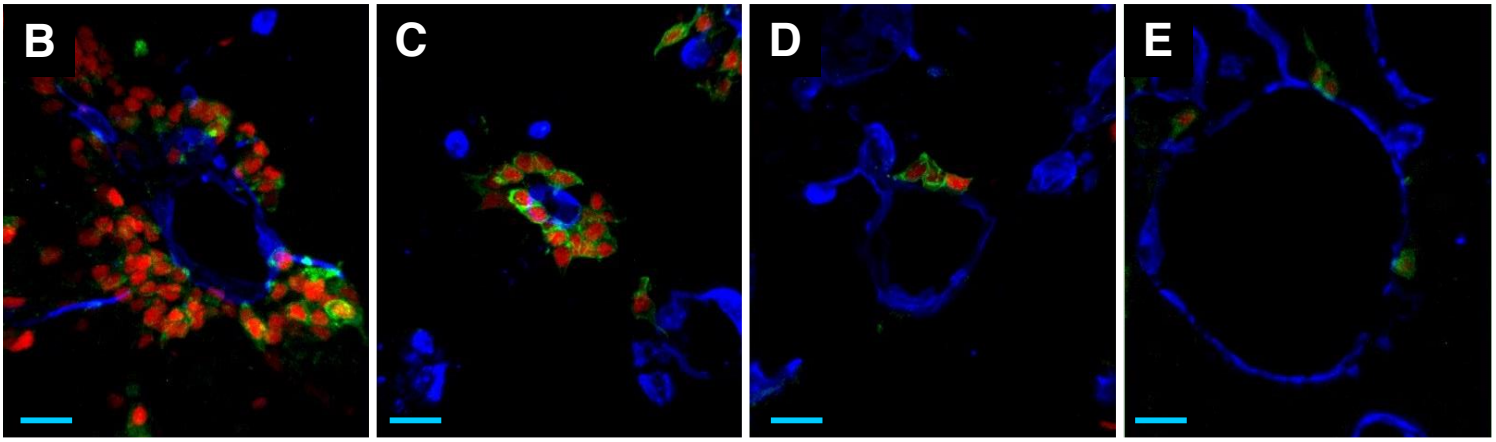

E15.5 explant, 10 μM Y27632

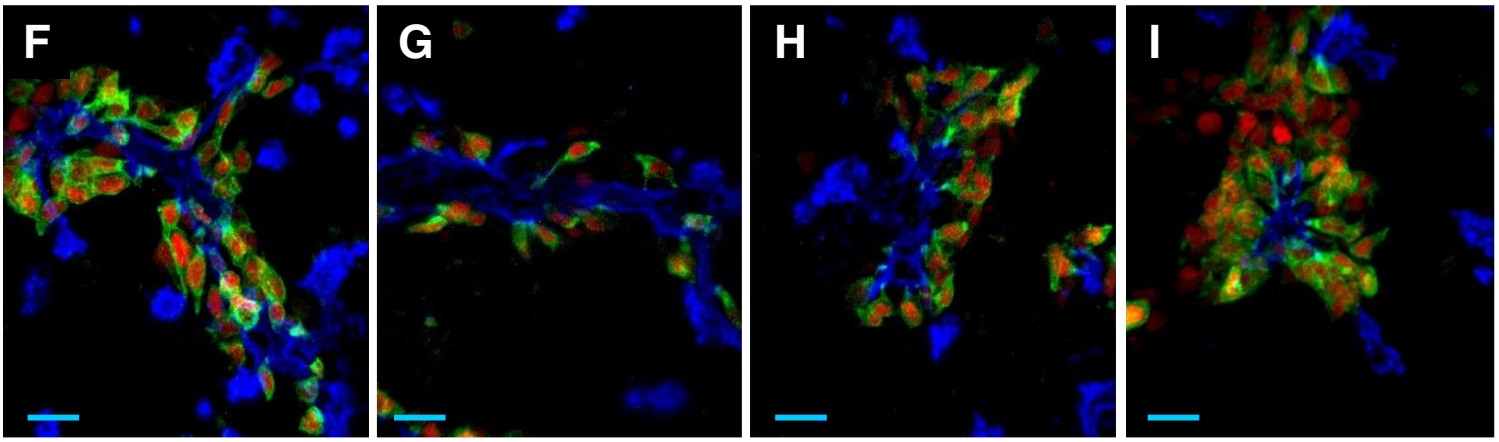

Muc1 mCherry GFP-GPI

Fig. S14. ROCK-nmMyoII pathway inhibitors influence lumenal expansion, apical narrowing, and basalward migratory processes during *Neurog3* activation and upregulation. (A) Muc1^{+} lumen morphology and *Neurog3*$^{RG+}$ cell morphology in untreated, BBS-treated (B-E), and Y27632-treated (F-I) explants. Scale bars are 15 μm.

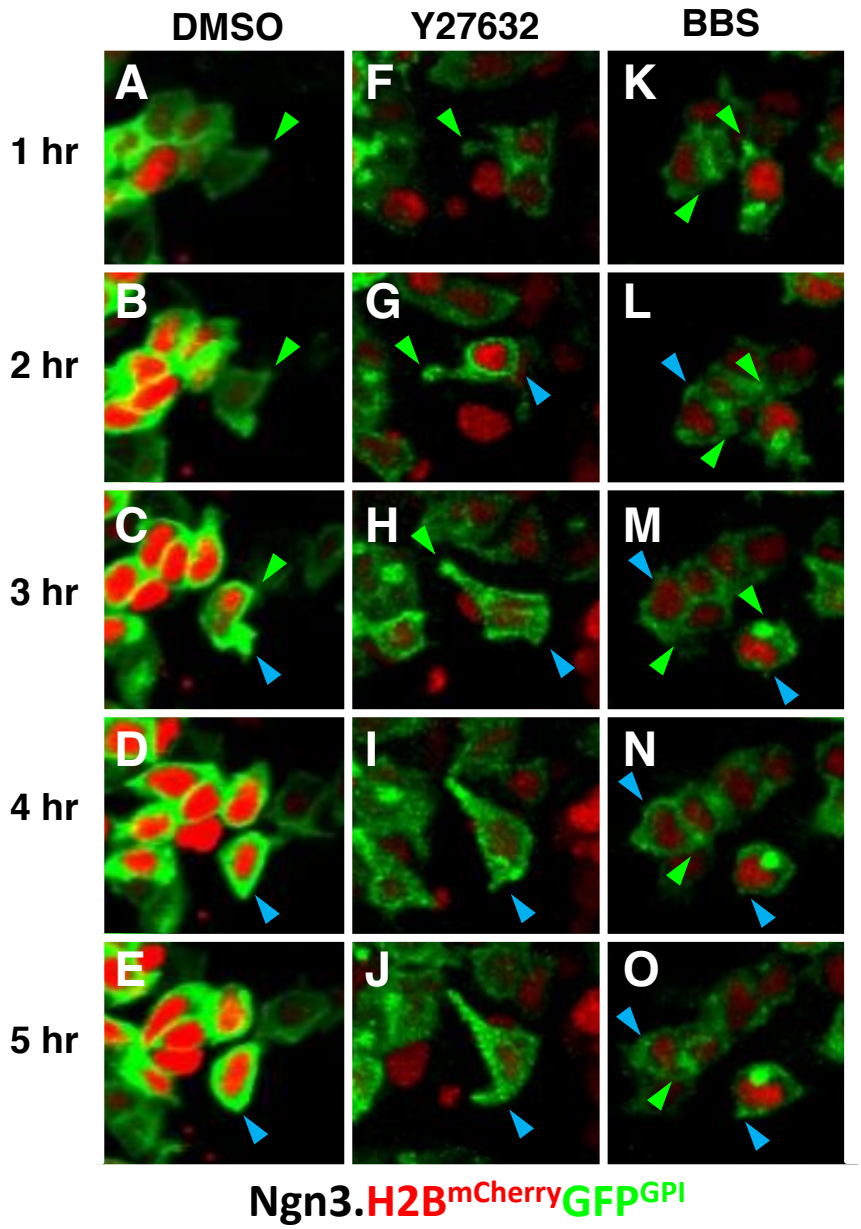

Fig. S15. Still frames from live imaging of endocrine-cell birth under nmMyoII- and ROCK-inhibited conditions. Still frames taken from time-lapse imaging experiments of *Neurog3*$^{RG+}$ cells cultured in vehicle alone (A-E), Y27632 (F-J), or BBS (K-O). Snapshots were extracted at one-hour intervals marked after commencement of imaging, which begins between 1-2 hours after drug administration. N = 1 for each condition. Green arrowheads mark the apical aspect of the *Neurog3*$^{RG+}$ cell. Blue arrowhead marks the basal surface of *Neurog3*$^{RG+}$ cells.

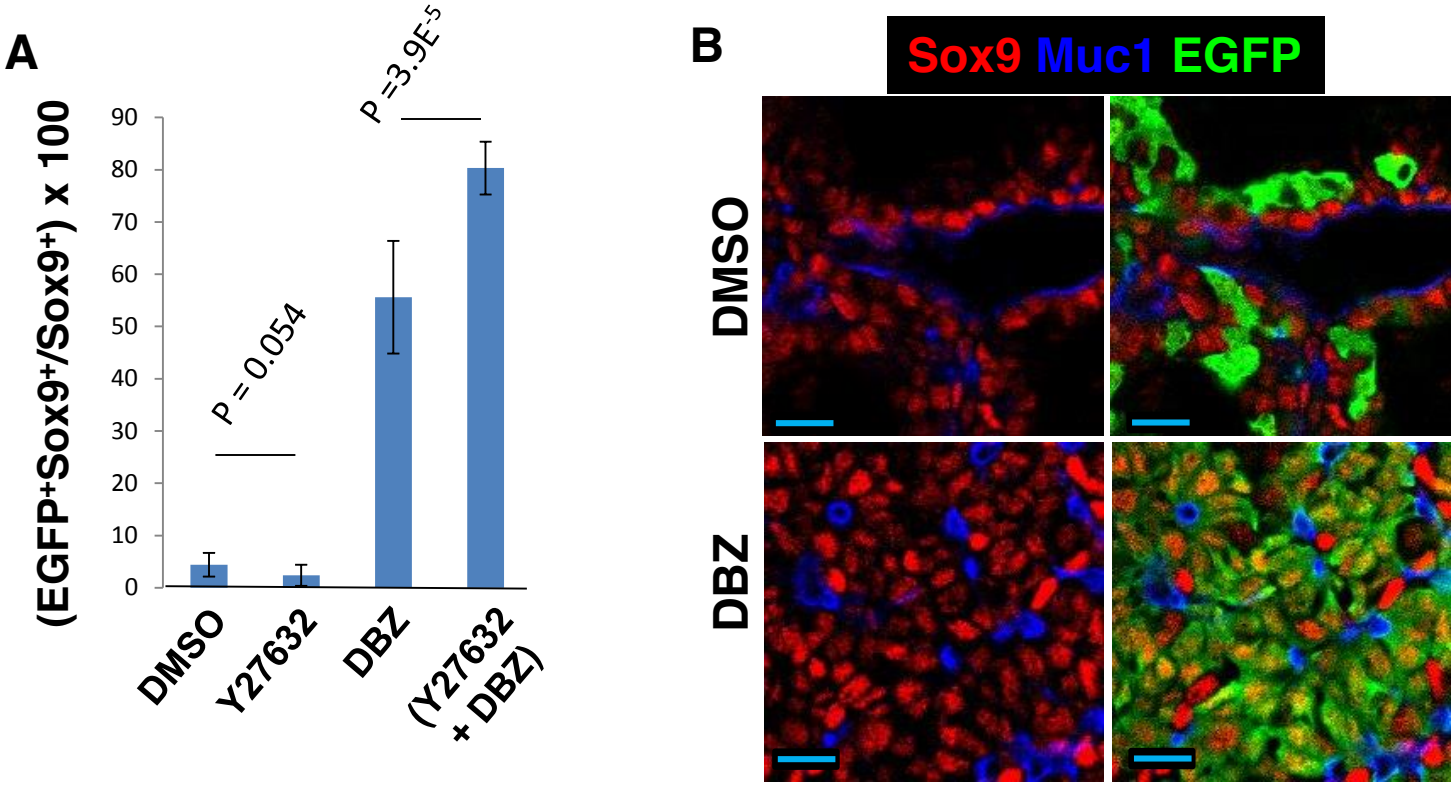

Fig. S16. ROCK and Notch inhibit *Neurog3* upregulation through distinct mechanisms. (A) Quantification of the proportion of Sox9^{+} epithelial cells that upregulate *Neurog3* in response to ROCK inhibition, Notch inhibition, or both in combination, in *Neurog3*$^{EGFP/+}$ explants. Note that ROCK inhibition has little to no effect in promoting *Neurog3* upregulation unless Notch signaling is inhibited. (B) Images of Sox9 and EGFP in DMSO and DBZ-treated *Neurog3*$^{EGFP/+}$ explants. Note the large number of Sox9^{+} and EGFP^{+} cells in the DBZ treated condition, which are only rarely observed in control tissue. Scale bars are 10 μm.

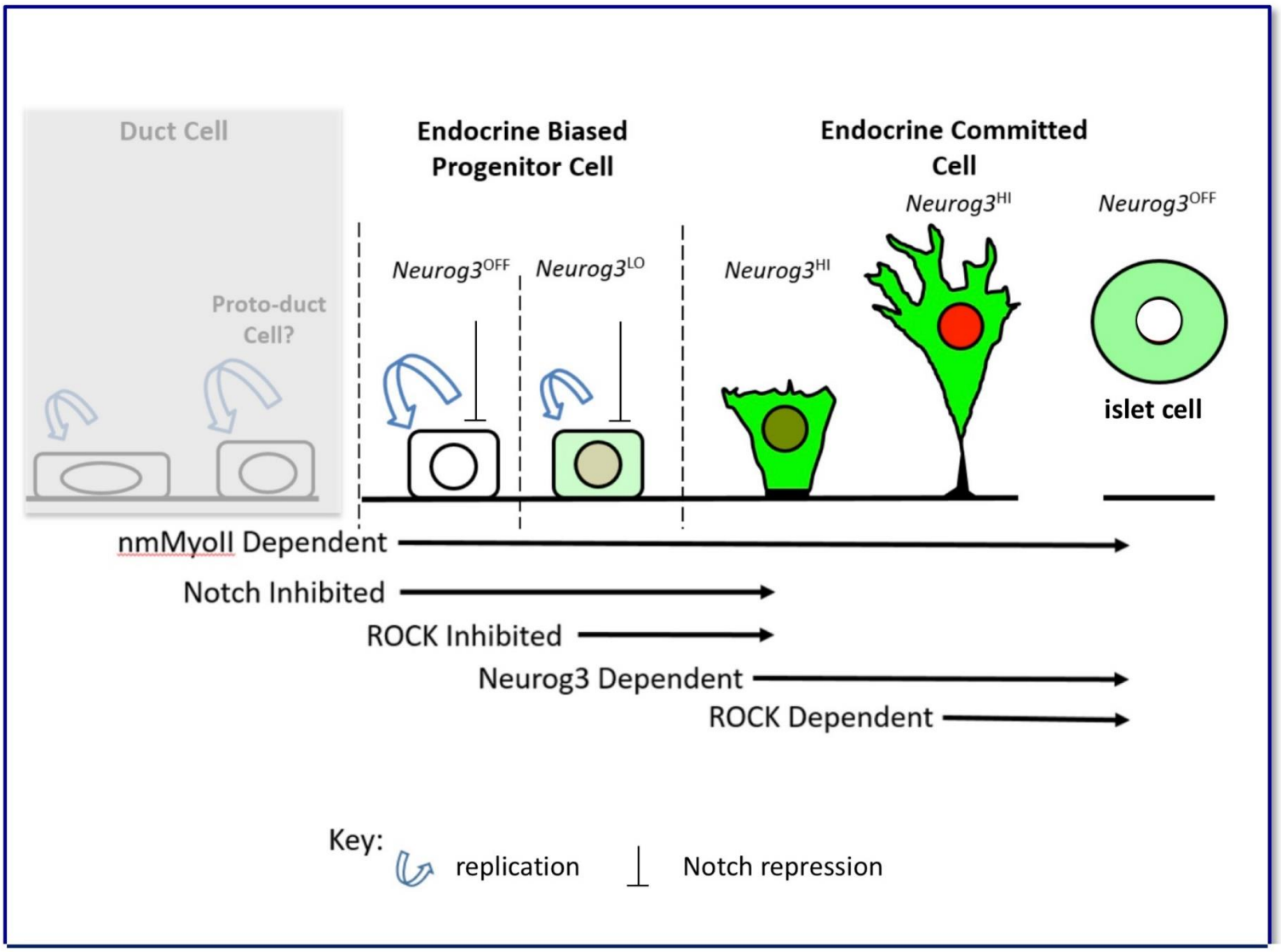

Fig. S17. Schematic of sequential steps in endocrine cell birth regulated by ROCK-nmMyoII, Notch, and Neurog3.

Table S1. Genotyping primers

Neurog3^{EGFP}		
Ngn3-1		
Ngn3-2	5'-ATACTCTGGTCCCCCGTG-3'	Lee et al., 2002
EGFP	5'-TGTTTGCTGAGTGCCAATC-3'	Lee et al., 2002
Neurog3^{FLOX}	5'-GAACTTGTGGCCGTTTACGT-3'	Lee et al., 2002
722	5'-CTATCCACTGCTGCTTGTCACTG-3'	Wang et al.,2008
723	5'-TGTGTCTCTGGGGACACTTGGAT-3'	Wang et al.,2008
Jv45	5'-TTCCGGTTATTCAACTTGCACC-3'	Wang et al.,2008

Table S2. Antibodies

Antigen	*Source*	*Dilution*	*Method*	*Company*
Muc1	Hamster	1:1000	Indirect IF	NeoMarkers
Sox9	Rabbit	1:5000	Indirect IF	Millipore
Neurog3	Goat	1:40,000	Biotin amplification	G. Gu (Vanderbilt)
EdU				Molec. Probes
Pdx1	G. Pig	1:1000	Indirect IF	C. Wright (Vanderbilt)
Ecad	Rat	1:2000	Indirect IF	AbCam
EGFP	Chick	1:2000	Indirect IF	Aves
DAPI			Mounting Medium	Life Tech.
Phalloidin		1:400	Direct Label	Molecular Probes
ZO-1	Rabbit	1:100	Indirect IF	Invitrogen
aPKC	Rabbit	1:400	Indirect IF	Santa Cruz
p-nmMyoII	Rabbit	1:200	Biotin Amplification	AbCam
nmMyoIIA	Rabbit	1:500	Indirect IF	Biolegend
nmMyoIIB	Rabbit	1:500	Indirect IF	Cell Signaling
γ-tubulin	Rabbit	1:1000	Biotin Amplification	AbCam
Prox1	Rabbit	1:1000	Indirect IF	AngioBio